Egypt. J. Chem. Vol. **68**, No.11, pp. 565- 593 (2025)

Egyptian Journal of Chemistry

http://ejchem.journals.ekb.eg/

Design, Spectroscopic Analysis, DFT Calculations and Biosorption Evaluation of Pristine Ostrich Bone Biosorbent towards efficient removal of hexavalent chromium and flavoring and coloring agents from wastewater in single and multi-contaminant systems

Doha MM Elawady[1], Elsayed RH El-Gharkawy[1] and Magda A Akl[1]*,

[1]*Department of Chemistry, Faculty of Science, Mansoura University, Mansoura 31556, Egypt*

Abstract

This research describes using pristine ostrich bone wastes (OB) as a biosorbent to adsorb several Azorubine (E122), Ponceau 4R (E124), and Red Allora (E129) dyes, as well as the hexavalent chromium ion Cr(VI). The physicochemical properties and morphology of OB biosorbent were investigated using BET, SEM, FTIR, TGA, ^{1}HNMR, and XRD. The impact of experimental parameters on the removal behavior of the pollutants under study was evaluated by adjusting the contact time, adsorbent amount, solution pH, temperature, and concentration. The adsorbate removal on OB biosorbent was obtained in the following order: E124> Cr(VI)> E122> E129. The adsorption kinetics of the investigated pollutants have been studied for single and multicomponent systems in terms of pseudo-first- and second-order kinetics. Freundlich and Langmuir isotherm models have also been applied to the equilibrium adsorption data. The outcomes demonstrated that the adsorption process adhered to a pseudo-second-order kinetic model was exothermic spontaneous. With the highest adsorption capacity, the Langmuir model provided the greatest fit to the sorption isotherm data at 303 K, being 85.66 mg/g, 86.67 mg/g, 157.76 mg/g, and 180.4 mg/g, for E129, E122, Cr(VI), and E124, respectively. Additionally, DFT calculations were utilized to verify the molecular structure, analysis of Frontier Molecular orbitals (FMOs), molecular electrostatic potential (MEP) and reactivity descriptor for all phases. The plausible mechanism of adsorption of the pollutants onto OB biosorbent is elucidated.

Keywords: Ostrich bone; Adsorption; anionic food dyes; Cr(VI); DFT calculations.

1. Introduction

The harmful effect of releasing hazardous materials in water, such as dyes, into the environment globally addresses the issues of water scarcity and toxin-induced water pollution [1]. Numerous industries like plastics, paper, textiles, and cosmetics utilize dyes to color their merchandise [2]. There are dyes in some organic and inorganic components of wastewater because of their complicated chemical structure, which protects them from light, oxidation, and biodegradation processes [3]. They are dangerous, degrade water transparency, and decompose slowly in water treatment facilities or landfills [4].

Food safety is a major concern for human life. The Food and Drug Administration (FDA) has authorized more than 3,000 substances as safe food additives used to thicken, color, preserve, or flavor food products. Many of these chemicals are prohibited because of the reported unforeseen negative effects. There are instances where food adulteration and additives lead to health hazards that include hyperkinesis, tumors, skin rashes, migraines, asthma, sleep disturbances, and stomach discomfort. Trendy dietary supplements often include artificial or natural flavorings and colors. Their use has also expanded recently since people are less aware of the risks connected to these agents. Health problems ranging from skin allergies and respiratory disorders to hormone imbalances and even some types of cancer have been linked to exposure to hazardous colors [5]. The majority of foods that are artificially colored contain petroleum-based chemicals and artificial food coloring, which do not naturally cur [6]. Food companies use Ponceau 4R (E124), Azorubine (E122), and Red Alora (E129) in samples like (pizza, macaroni, candies, soft drinks, and cheese) because of their physicochemical and thermal stability as well as their symmetry in aromatic groups, which leads to their high strength [7]. Food color consumption is increasing, especially in children. Overindulging in food dyes contaminated with pollutants may harm one's health. To counteract their negative effects, they must be eliminated [8].

Coal mining, agriculture, household garbage, and the leather industry are some of the point and non-point sources of heavy metal ions that can enter waterways. Unfortunately, when these harmful heavy metals seep into soil and water, they can endanger people and animals.

---

*Corresponding author e-mail: magdaakl@yahoo.com.; (Magda A Akl)

Receive Date: 07 February 2025, Revise Date: 09 March 2025, Accept Date: 20 March 2025

DOI: 10.21608/ejchem.2025.358578.11278

The heavy metal chromium (Cr) is widely used and is known to be toxic in the natural environment. It is vital to remove heavy metals before discharging them since they can accumulate in living tissues and cause a variety of illnesses. Unlike organic waste, heavy metals do not biodegrade [9-10]. Chromium (Cr) compounds find application in a wide range of sectors, such as textile dying, tanneries, and metal electroplating. Chromium(VI) is regarded as extremely reactive owing to its severe reactivity and potential for carcinogenicity [11]. In addition to liver and kidney damage, dermatitis, internal bleeding, nausea, diarrhea, and respiratory issues, acute exposure to Cr(VI) can also induce these side effects [12]. Asthma, nasal septal ulceration, inflammation, and acute poisoning can all result from inhalation [12]. The liver and kidneys may be impacted by ingestion. In addition to interfering with the healing of cuts or scrapes, skin contact can cause severe burns or even systemic poisoning. It can cause ulceration and serious consequences if left untreated.

At the moment, removing these pollutants from wastewater involves several methods, such as precipitation, biological oxidation, ion exchange, flocculation/coagulation, adsorption [13], advanced oxidation process (AOP), biodegradation, and other techniques that are being created to reduce wastewater's dye content [14]. The low cost, high effectiveness of color removal from diluted solutions, design versatility, and insensitivity to dangerous contaminants make adsorption techniques very appealing [15]. The technical and financial feasibility of the procedure depends on the choice of adsorbents [16]. Biosorbents, natural materials, and agricultural industry wastes are examples of unconventional adsorbents that can be used in wastewater decontamination.

The bioproducts of meat and bone meal obtained by crushing animal corpses to remove fat are produced by animal slaughter and the food industry [17]. Ostrich bone can effectively remove Organic and inorganic anions, which is regarded as a cheap and plentiful adsorbent [18]. Calcium phosphate and collagen fibers make up most of the makeup of ostrich bones, just like in other birds [19]. Together, these two elements provide the skeletal framework strength and flexibility. The hardness and rigidity of bones are derived from calcium phosphate in the form of hydroxyapatite crystals [20]. Nevertheless, OB has a restricted application due to the challenges associated with separation and recycling. Due to their high adsorption capability, accessibility, and affordability, animal bones have garnered significant attention recently for the removal of pollutants [21]. 30% of the weight of bones is organic, while 70% is made up of inorganic substances. Calcium and phosphate found naturally in hydroxyapatite, or $Ca_{10}(PO4)_6(OH)_2$, make up the majority of the inorganic components of bone. [22-23]. Ostrich bone, which is generated in large amounts, can be used in place of commercial absorbents [24]. An adsorbent is a material that is often porous and has a large surface area that allows substances to be adsorbed onto it by intermolecular interactions [25]. Animal bones are dried to create a porous, granular, white substance known as animal bone. As the intake of meat rises, more bone will be generated as solid waste, which is harmful to the ecosystem [26]. To remove contaminants from wastewater and effluent gas, waste bones can be used as an adsorbent [27]. Bone biochar's exceptional physicochemical qualities, large surface area, and pore volume make it a popular adsorbent for the remediation of water contamination [28]. Numerous research studies conducted over the past few decades have documented the use of bone biochar to remove a wide range of organic and inorganic contaminants from aqueous solutions [29-33]. It is considered that one of the major challenges faced with adsorption by activated carbon is its cost-effectiveness. So, the research of recent years mainly focused on utilizing natural materials [34]. In this study, pollutants [E122, E124, E129, and Cr(VI)] were removed from the aqueous solution by applying a stable immobilized cationic biosorbent and an anionic adsorbate to the surface of ostrich bone. For the first time, this work provides a flexible and gentle technique for immobilizing adsorbate on the surface of an ostrich bone, a biological origin support. A literature survey proved that the removal of anionic food dyes (E122, E124, E129) or Cr(VI) has never been published before. Furthermore, the molecular structure, electronic properties, theoretical spectral properties (IR), and any quantum mechanical calculations of OB, OB-E122, OB-E124, OB-E129, and OB-Cr(VI) have not been reported in the literature review. This work examined the spectrum features, electronic and molecular characteristics, and some quantum mechanical computations of OB biosorbent, OB-E122, OB-E124, OB-E129, and OB-Cr(VI).

Result and Discusion

2.1 Materials, design and physicochemical studies

2.1.1. Digital images

Fig. 1(a, b, c, d, E) represents the digital images of OB before adsorption of pollutants, OB-E122, OB-E124, OB-E129, and OB-Cr(VI), respectively.The color of the pristine OB material changed from off-white **(Fig. 1a)** to light red in case of OB-E124 **(Fig. 1b),** allura red in the presence of OB-E129 (**Fig. 1c**), solid red in case of OB-E122 **(Fig. 1d),** and to yellow in case of OB-Cr(VI) **(Fig. 1E).**

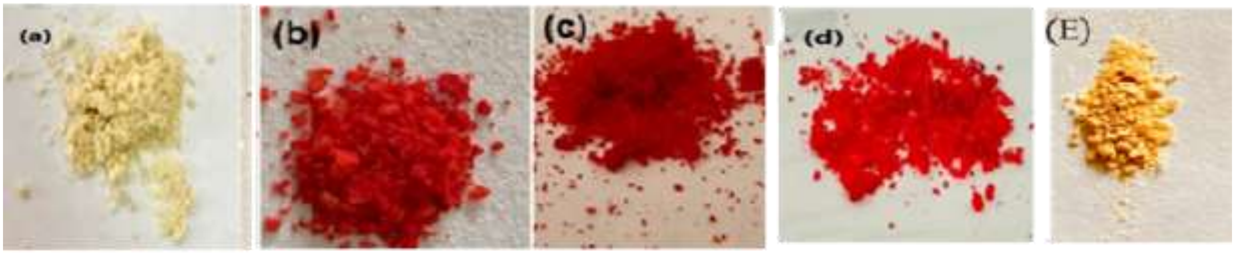

Figure 1. (a) OB before adsorption; (b, c,d) digital images of anionic dyes after adsorption on OB, and (E) digital image of OB-Cr(VI).

2.1.2. BET analysis

The textural properties of the samples, evaluated from low-temperature nitrogen adsorption, are given in Table 1 and graphically represented in **Fig. S1**. The great specific surface area (156.745 m2/g) and average pore size (28.5 Å) of OB give an increase in the approachability of the active sites of the adsorbent in contact with the contaminated water, which leads to a better efficiency of the OB in the removal of pollutants. The average pore size (28.5 Å) of OB is greater than the atomic radius of Cr (1.4 Å). A finding can explain the easy particle diffusion of the studied pollutants.

Table 1. The BET-specific surface area and pore size of bone.

Total surface area m²/g	156.745
Total Pore Volume (cc/g)	0.223
Average Pore Size (Å)	28.85
Average Particle radius 8.6997e+000 nm	8.6997e+000

Characterization

1.1.1. SEM/EDX

The SEM images revealed that the (OB) biosorbent particles have irregular shapes and sizes, with edges and corners that might be due to the grinding effect during preparation, which enables the pollutants on its surface to be adsorbed **Fig. 2(a, b, c)**. The organic/inorganic content of the bone tissue and biomaterial granules was measured using EDX. The qualitative and semiquantitative element contents (weight % and atomic %) were evaluated as presented in **Fig. 2d**. For all spectra, the presence of calcium (Ca) and phosphorous (P) were evaluated. The table inside **Fig. 2d** illustrates the EDX analysis of OB. From the results shown therein, the weight percentages of Ca and P are 6.68% and 2.9%, respectively. This confirms the presence of the hydroxyapatite compound in the OB biosorbent.

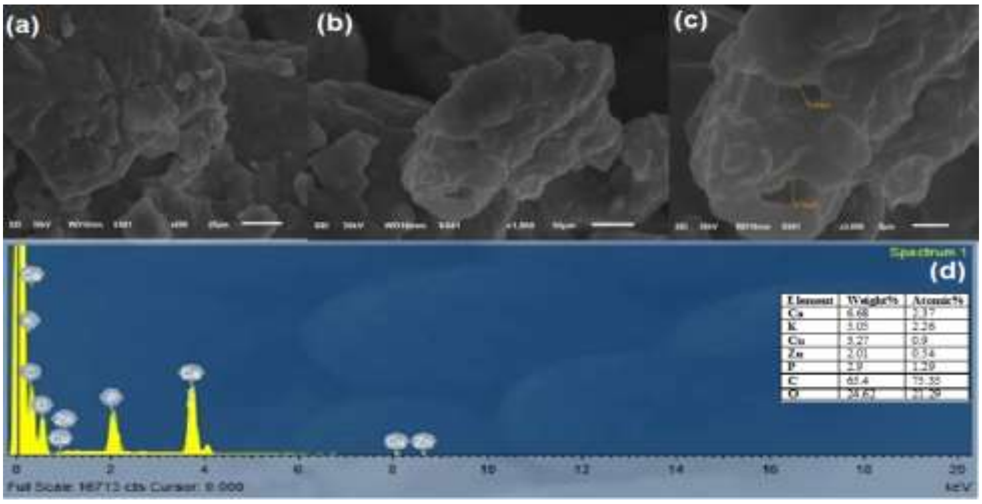

Element	Weight%	Atomic%
Ca	6.68	2.37
K	3.05	2.26
Cu	3.27	0.9
Zn	2.01	0.54
P	2.9	1.29
C	65.4	75.35
O	24.67	21.29

Figure 2. (a), (b), (c) The surface images of Ostrich bone at different magnification scales, and (d) EDX analysis of OB.

2.2.2. FTIR spectra

The FTIR spectra of the OB biosorbent are displayed both just before and after the pollutants are adsorbed in **Fig. 3** and were obtained and studied in the range of (500 cm^{-1}- 4000 cm^{-1}) samples with the given bands; about (II) $(-CO_3)^-$, the band intensity appears at 1014.54 cm^{-1}; whereas the band at 1636 cm^{-1} is related to organic tissue and water of ostrich bone. The pristine OB shows a characteristic absorption band of symmetric and asymmetric stretching vibrations of the CH_2 and CH_3 groups at around 1455-1470, 2852.21, and 2914 cm^{-1}. The spectrum in the C-H stretching region shows an absorption maximum at 3293 cm^{-1}, which is typical of the C–H stretching vibration of the aromatic rings. The characteristic vibration peaks of O–P–O bonds of calcium phosphate appeared in the sample 1161.23 cm^{-1} ((II) HPO_4^- group, P–O–H in-plane and out-of-plane deformation modes), 1014 and 1161 cm^{-1} (v3, P-O asymmetric stretching vibrations) the FTIR also shows an indication of the inorganic phase of the bone by two bands in the 1014-1161.23 cm^{-1} region attributed to HAP, whereas amorphous calcium phosphate appears as a broad single band. The high organic phase content of ostrich bone may be why the distinctive HAP vibration bands are barely visible in the bone. HAP vibrations from 1235 cm^{-1} and 1000 cm^{-1} indicated that the HAP content has Ca-O in the OB structure.

In the FTIR spectrum of OB-E122, the symmetric stretching vibrations of the (S-O) bonds form of the $S0_3^-Na^+$ (sulphonic acid salts) of the $R\text{-}SO_3^-\ Na^+$ group were responsible for the absorption lines at 1024 and 559.7 cm^{-1}, respectively. The vibrations of the O-H group were responsible for the absorption lines at 3409, 1336, 686, 602, 599, and 568 cm^{-1}, and the N=N [18].

Furthermore, the FTIR spectrum of OB-E124 has the same lines at 3450.02 cm^{-1},1022 cm^{-1} attributed to the O-H group, symmetric stretching vibrations of the (S-O) respectively, and an absorption line at 1630,1512.11 cm^{-1} credited with C-N, N=N respectively [16], and the FTIR of OB-E129 has lines at 3449, 3439 cm^{-1} attributed to O-H group, lines at 1023, 538 cm^{-}

^{1} were attributed to symmetric stretching vibrations of the (S-O) bonds form of the $SO_3^-Na^+$ (sulphonic acid salts), and 1581cm^{-1} lines attributed to C-N group [20].

The FTIR spectrum of pure potassium dichromate has a characteristic peak at 1111.5 cm$^{-1,}$ which appears at 1156 cm^{-1} as mentioned in the literature [35]. It is seen from the spectrum that the $(Cr_2O_7)^{2-}$ stretching frequency of $K_2Cr_2O_7$ is shifted from 1111.5 into 1319.15 cm^{-1} in **Fig. 3c**. The more intense and broader (3047-3667) cm^{-1} vibrations of the bonds of the O–H group and the vibrational peak at 2914 cm^{-1} is attributed to $-CH_2$ and $-CH_3$ and Cr(VI) having characteristic bonds around 800 cm^{-1}. The FTIR spectra of OB after the adsorption of dyes is the confirmation that there is an interaction between the pollutants and OB. The band vibration at 1541 cm^{-1} indicates C=C; furthermore, the formation of the peak at 1400 cm^{-1} which is a characteristic bond of S=O and there is a shift in peaks from 1013 to about [1022-1024] cm^{-1} which indicates the electrostatic interaction between Ca from HAP and oxygen from sulphonic acid in the dye molecule, and the broadness increases at 3036-3613 cm^{-1} which means the formation of intermolecular hydrogen bonding.

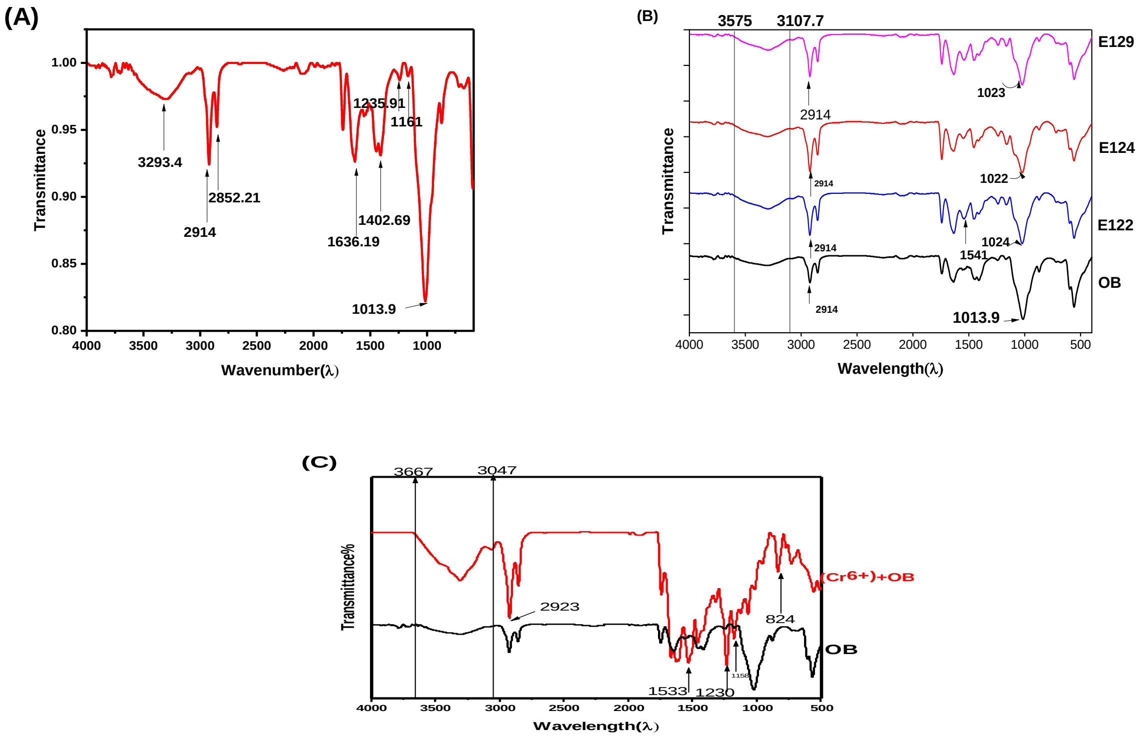

Figure 3. IR Spectrum of (A) OB biosorbent before adsorption, (B) OB after adsorption of (a) E122, (b) E124, and (d) E129 dyes, and (C) OB after adsorption of Cr(VI).

2.2.3. XRD analysis

The X-ray diffraction patterns of pristine ostrich bone are given in **Fig. 4.** Comparison of the XRD pattern to the JCPDS confirms the presence of a major calcium hydroxyapatite (CaHAP) phase $[Ca_{10}(PO_4)_6(OH)_2]$ as compared with the XRD standard card. At the same time, the broad and intense background was attributed to collagen, fat tissues, and other organic compounds [22]. The key diffraction peaks of the OB were shown in the XRD patterns, roughly showing the crystallinity of OB at 19.28°, 25.79°, and 28.86° with major intensity at peak value 32.29° with a corresponding plane (211). This primary peak was discovered to be related to OB as shown in **Fig. 4**. Small deviations of these peaks from standard values may be due to a slight number of foreign ions like (Zn^{2+} and Cu^{2+}) This result of XRD analysis obtained in the present investigation is in good agreement with the reported results in EDX analysis.

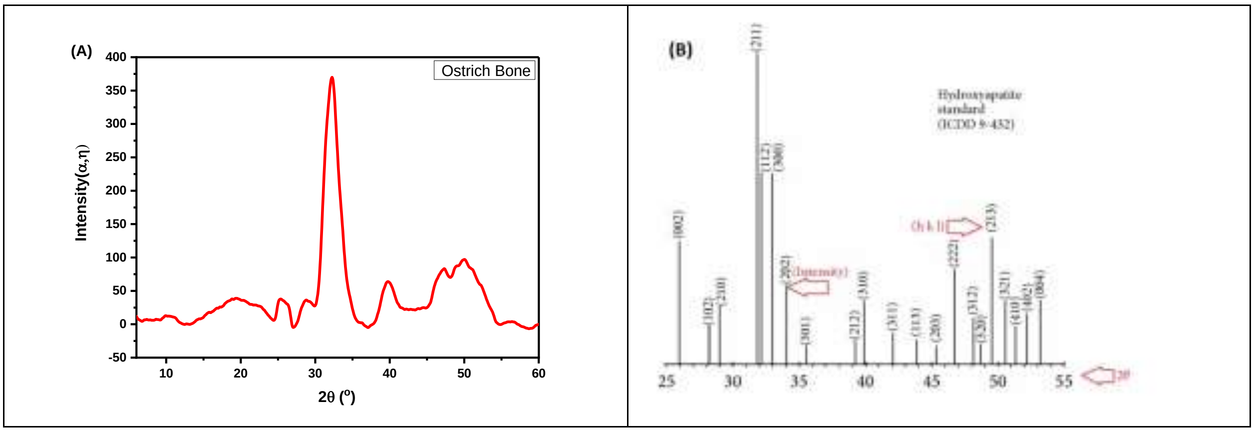

Figure 4. (A) The XRD patterns of the OB sample (B) The hydroxyapatite XRD standard card.

2.2.4. ^{1}HNMR analysis

Deconvolutions of the data have been done by empirically selecting the peak positions and assuming a Gaussian shape profile of the peaks at around 0 and 5.25 ppm, respectively. **Fig. 5** provides a summary of the findings. When comparing the NMR peak near 0 ppm with the value of 0.2 ppm reported in the literature, it is attributed to the hydroxyl group in HA and is detected at substantially up-field regions [23]. Such results are well-known in the literature for HA ceramics with colloidal dimensions [24]. One can expect resonance due to the acid phosphate group (HPO_4) at the same position, i.e. 5.25 ppm.

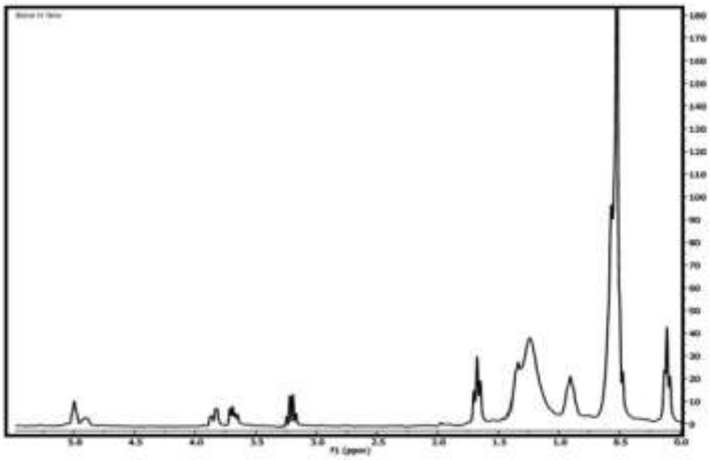

Figure 5. ^{1}HNMR of OB biosorbent.

2.2.5. TGA

The OB biosorbent underwent three phases of weight loss, as revealed by thermal analysis (TG). Stage I (81.9–231°C) is related to the desorption of physically retained water (3.3 wt%), with mainly the attracted and loosely bound water removed from the inward framework and surface of the bone. Stage II (231– 494.5°C), is a process of fast degradation and burning of organic components (bone marrow, fat tissue, and collagen are pyrolyzed to water and carbon dioxide) and the liberation of some strongly bound crystal water. In the third stage (494–800 °C), the weight loss decreased at a lower rate than in stage II, and the weight loss was very slow above 625 °C (14.0 wt%). The additional weight loss in stage III could be explained by several phenomena, one of which is the burning of the residual organic components, the oxidation of carbon from the framework of the bone to carbon dioxide, and the release of possible lattice water [23]. According to TGA analysis **Fig. S2**, the elimination of the organic part and the mass loss of annealed ostrich bone were verified. The loss of water and organic matter is represented by the two inflection points in the TGA curves for the ostrich bone, which were found at about 100 °C and 400 °C. As a result, organic elements such as adipose tissues, collagen, chondroitin sulphate, keratin sulphate, and lipids were completely removed from the bone below 600 °C. No discernible weight loss was seen between 500 °C and 800 °C. Studies have indicated that drinking water and eating organic foods can cause weight loss of about 34% [36]. The ostrich bone has consistently been cleared of substances, which indicates that bone comprises about 61% inorganic mineral crystals and about 39% corresponds to the organic phase consisting of collagen protein fibres.

2.3. DFT calculations

2.3.1. Optimized molecular geometry

The optimized geometry of the Ostrich bone (OB) unit, E122, E124, E129, Cr(VI), these pollutants, and Cr(VI) with product OB are shown in **Fig. 6.**

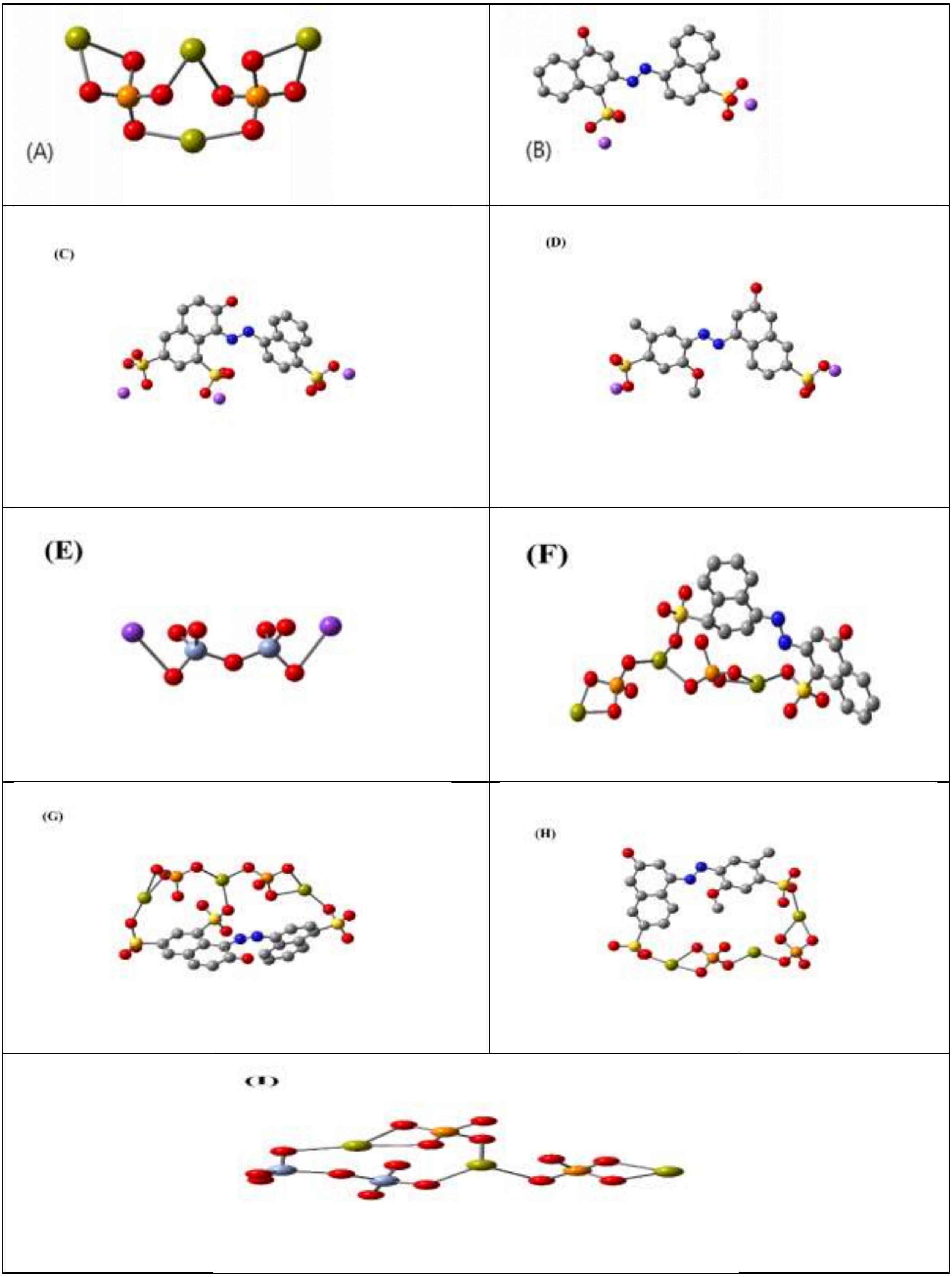

Figure 6. The optimized structures for (a) OB, (b) E122, (c) E124, (d) E129, (e)Cr(VI), and (f, g, h, I) are the product of OB+ E122, E124, E129, Cr(VI), respectively based on the DFT/ B3LYP/6–31g(d, p) methodology.

2.3.2. Molecular orbital properties and global reactivity descriptors(GRDs)

2.3.2.1. Global Reactivity Descriptors

A compound's Global Reactivity Parameters (GRDs) [37-39] can be predicted from the HOMO-LUMO gap. The HOMO is an electron donor and LUMO the electron acceptor sites are shown in **Fig. 7** for the Ostrich Bone (OB) unit, E122, E124, E129, Cr(VI), these anionic dyes, and Cr(VI) with product Ostrich Bone. From **Table 2,** the higher reactivity of the Ostrich Bone (OB), E122, E124, E129, and Cr(VI) is explained in the light of the energy gap, ΔE_{gap}, which measures the reactivity; as the energy gap decreases, the reactivity increases.

Additionally, the reactivity of ostrich bone with anionic dyes and Cr(VI) is evident from the results of their Egap and the amount of electronic charge transfer. The energy gap of soft molecules (σ) is tiny, but that of hard molecules (η) is significant [40, 41]. A soft molecule is more reactive than a hard molecule because a soft molecule has a lower $\Delta E_{(LUMO\text{-}HOMO)}$.

The χ is a measure of the power of atom(s) to attract the electrons from the other molecules [42]. A high electronegativity (χ) value for the dyes and chromate suggests a strong ability to attract electrons from Ostrich bone, leading to greater interaction to form the resulting compounds.

The ionization potential, I_P, and electron affinity, E_A, can be expressed as negative values of E_{HOMO} and E_{LUMO}, respectively. Ionization energy is a descriptor expressing the chemical reactivity of atoms and molecules. Greater stability and chemical inertness are indicated by greater ionization energy values and vice versa. Lower ionization energy denotes a higher level of atom and molecular reactivity [43]. **Table 2** shows the values of the ionization energy of the investigated molecules. The low ionization energy of OB indicates its high reactivity with anionic dyes and chromate ions (Cr(VI)).

According to the definition of the electrophilicity index (ω), t measures the tendency of chemical species to acquire electrons. The results of electrophilicity seen in **Table 2** are in decreasing order.

Finally, the dipole moment (μ) is a factor that can also provide information about the interaction between molecules. The (E_{HOMO}), (E_{LUMO}), energy gap $\Delta E_{(LUMO\text{-}HOMO)}$, ionization potential (IP), electron affinity (EA), hardness (η), softness (σ), electronegativity (χ), chemical potential (μ)The Global electrophilicity index (ω) and dipole moment in **Table 2** list the Cr(VI) ion before and after adsorption as well as the three anionic dyes before and after adsorption.

HOMO	LUMO
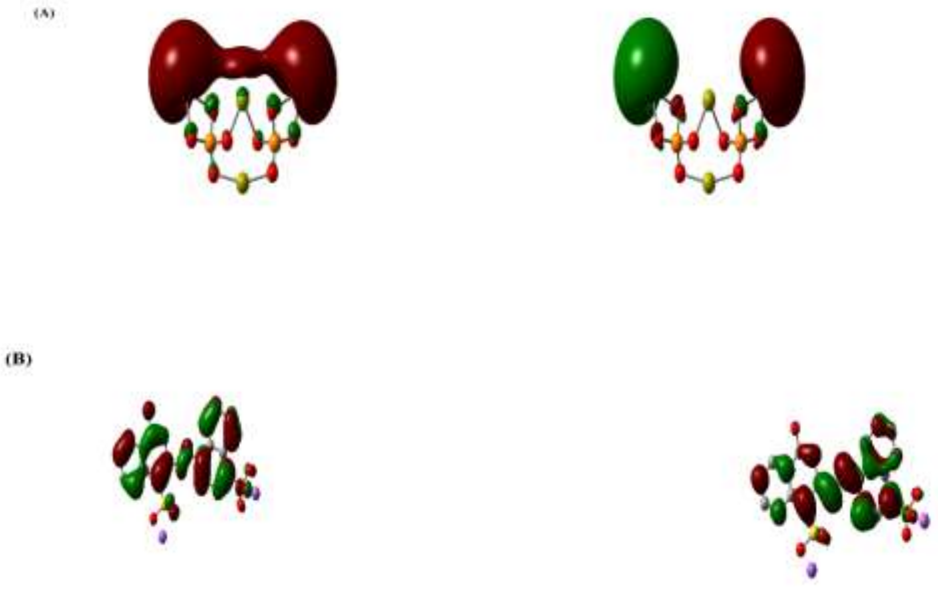	

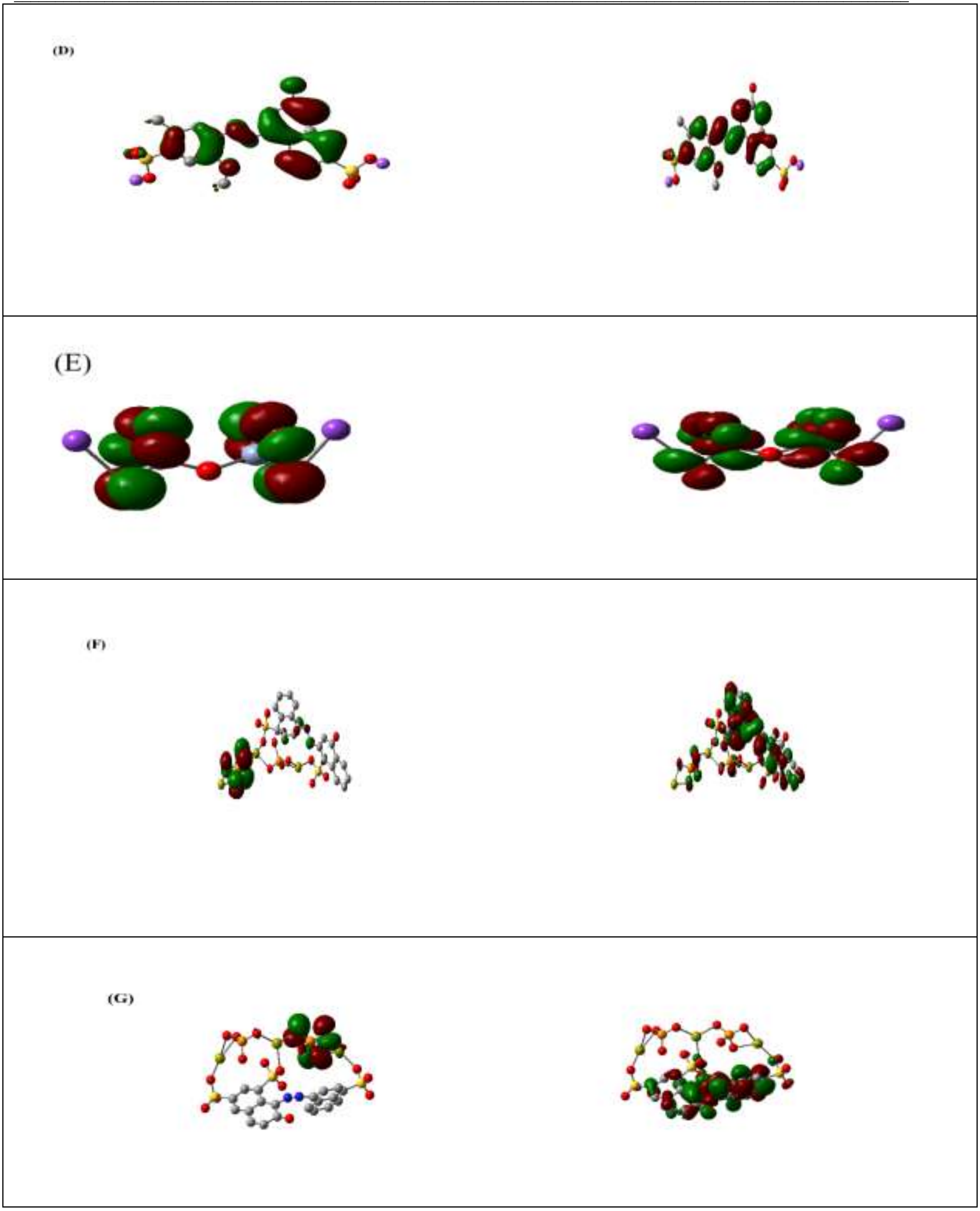
(D)
(E)
(F)
(G)

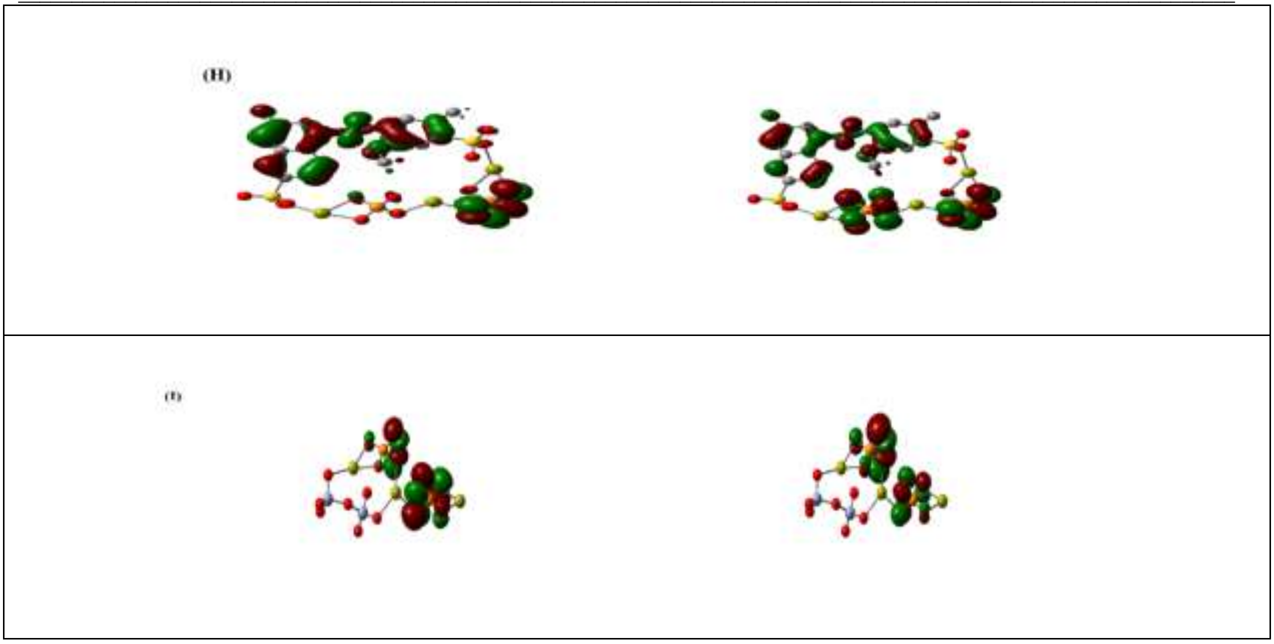

Figure 7. HOMO and LUMO structures for (a) OB, (b) E122, (c) E124, (d) E129, (e) Cr(VI), and (f, g, h, I) is the product after adsorption of E122, E124, E129, and Cr(VI) +OB respectively based on the DFT/ B3LYP/6–31g (d, p) methodology.

Table 2. The Global Reactivity Parameters were determined using the DFT/ B3LYP/6–31g (d, p) method of calculations for $Ca_4(PO_4)_2$, E122, E122 + OB, E124, E124 + OB, E129, Cr(VI), and OB+Cr(VI).

Property	**$Ca_4(PO_4)_2$**	**E122**	**E122 + OB**	**E124**	**E124 + OB**	**E129**	**E129 + OB**	Cr(VI)	Cr(VI) **+ OB**
E_{HOMO} [eV]	-0.12731	-0.19561	-0.18804	-0.19514	-0.26628	-0.19806	-0.23799	-0.2234	-0.25261
E_{LUMO} [eV]	-0.11125	-0.08102	-0.17598	-0.07605	-0.18932	-0.08213	-0.22438	-0.0581	-0.22697
ΔE_{gap} [eV]	0.01606	0.11459	0.01206	0.11909	0.07696	0.11593	0.01361	0.1653	0.02564
□ [eV]	0.00803	0.057295	0.00603	0.059545	0.03848	0.057965	0.006805	0.08265	0.01282
□ $[eV]^{-1}$	124.533	17.45353	165.8375	16.79402	25.98753	17.25179	146.9508	12.09921	78.00312
I_p [eV]	0.12731	0.19561	0.18804	0.19514	0.26628	0.19806	0.23799	0.2234	0.25261
E_A [eV]	0.11125	0.08102	0.17598	0.07605	0.18932	0.08213	0.22438	0.0581	0.22697
□ [eV]	0.11928	0.138315	0.18201	0.135595	0.2278	0.140095	0.231185	0.14075	0.23979
μ [eV]	-0.11928	-0.138315	-0.18201	-0.135595	-0.2278	-0.140095	-0.231185	-0.14075	-0.23979
ω [eV]	0.8859102	0.166952	2.7469022	0.1543875	0.6742833	0.1692971	3.9270025	0.1198461	2.2425602
The dipole moment [Debye]	3.2864	4.3449	11.2956	7.7487	9.6198	1.6293	15.688	6.2726	26.006

2.3.3. Infra-red spectra analysis

Infrared analysis is supported by theoretical computations, which allow for a trustworthy interpretation of experimental gaseous molecule spectra. B3LYP/6–31g (d, p) calculations are the most prominent method used to model IR spectra. The comparison is made between IR spectra calculated for gas phase molecules and those measured in the solid state. Furthermore, Asadi et al. report a comparison between gas phase DFT and condensed phase experimental data and obtained quite good agreement [44]. The IR spectra of the OB, E122, E124, E129, and Cr(VI) are displayed in **Fig. 8.**

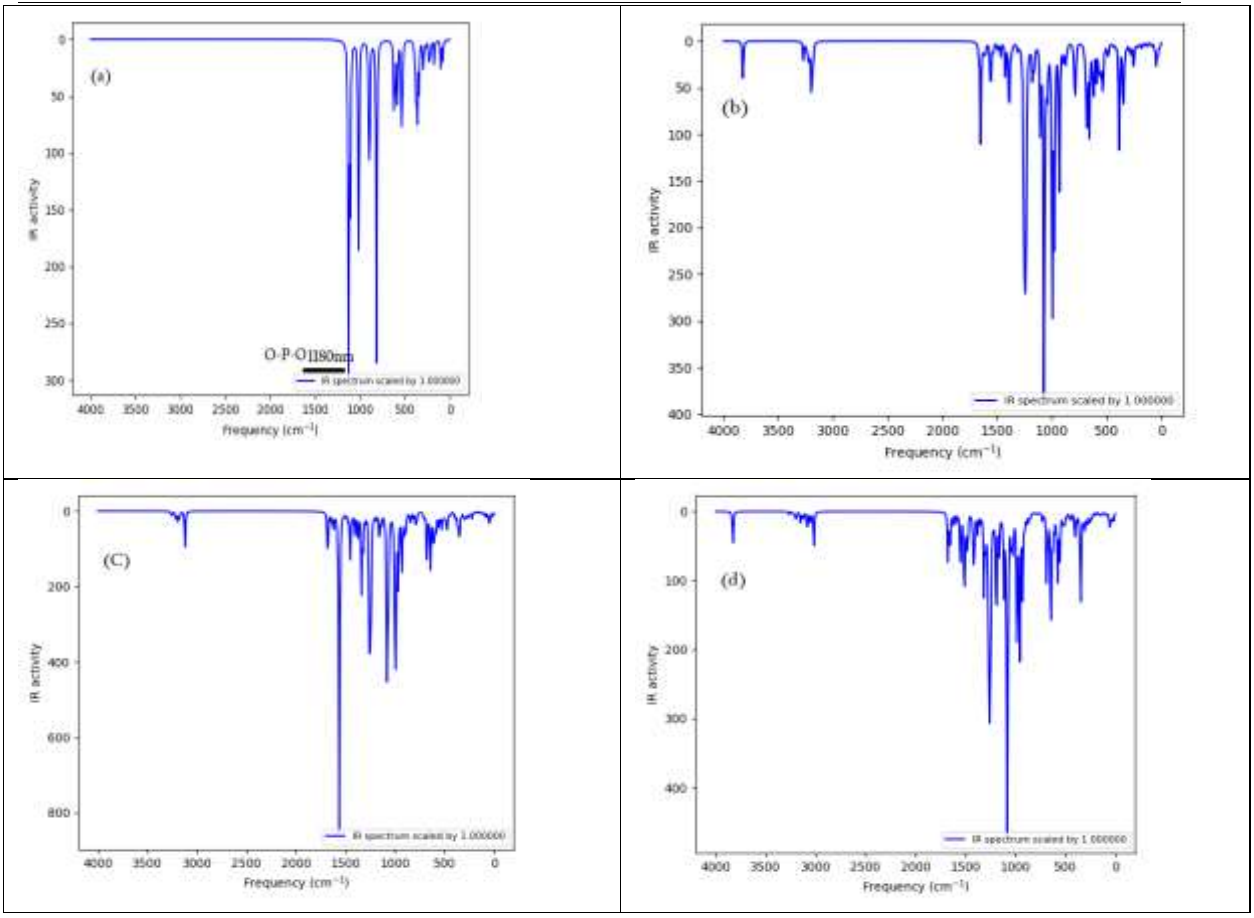

Figure 8. The calculated IR spectrum for (a) OB, (b)E122, (c) E124, and (d) E129 based on the DFT/ B3LYP/6–31g (d, p) methodology.

2.3.4. Molecular electrostatic potential (MEP)

The partial distribution of change along a molecule's surface is displayed by the electrostatic potential (ESP) surface or map. Three-dimensional representations of the charge distributions of molecules are provided by electrostatic potential maps, commonly referred to as molecular electrical potential surfaces or electrostatic potential energy maps. These maps give us the ability to see a molecule's variable charge areas. Understanding the charge distributions can be very helpful in determining the polarity of molecules as well as how they interact with one another. A color spectrum is used to represent the different intensities of the electrostatic potential energy values, with blue being the highest value and red representing the lowest, to make the electrostatic potential energy data easier to read. The calculated ESP maps of OB and three anionic dyes and chromate before and after adsorption are shown in **Fig. 9.**

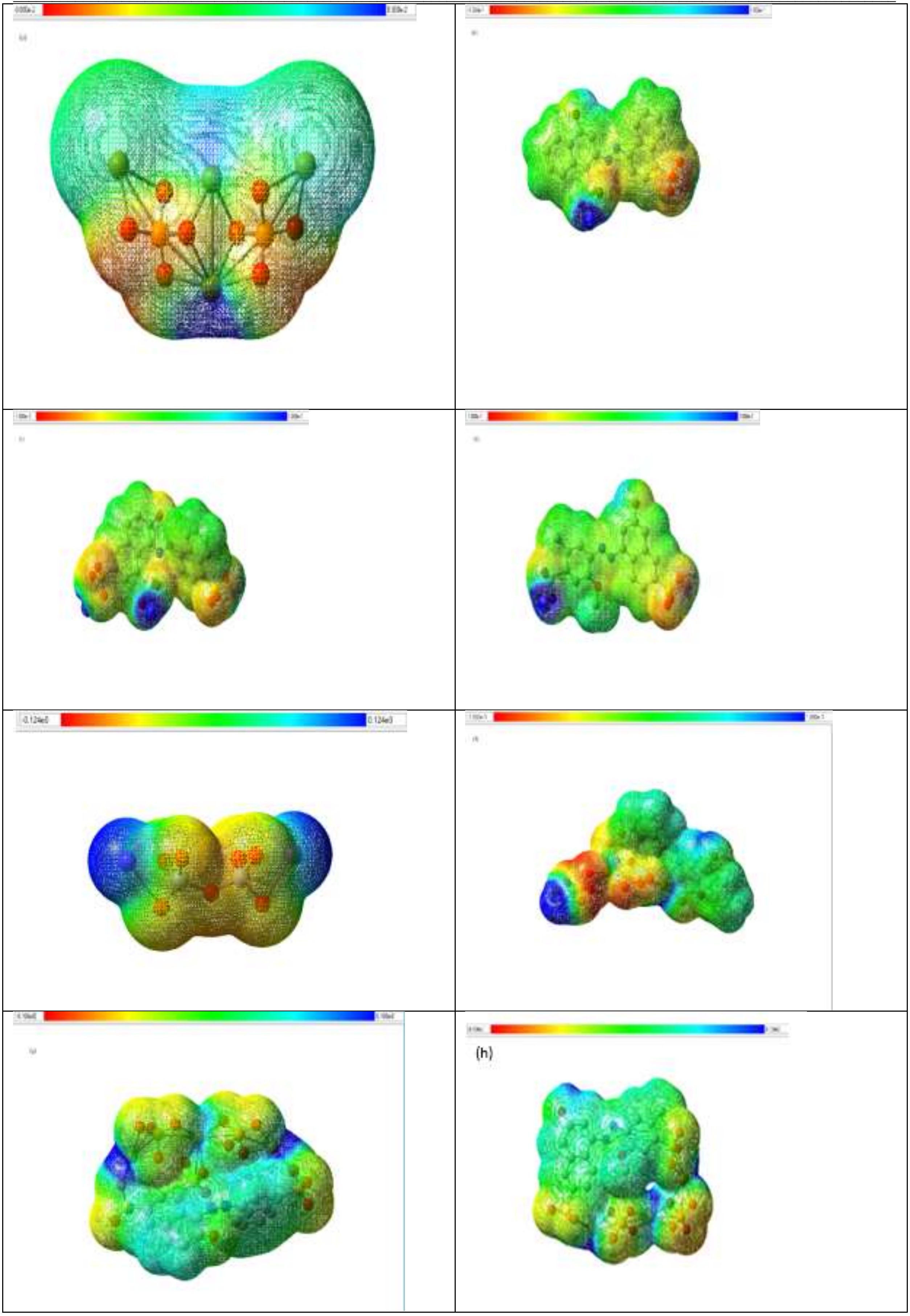
-0.124e0
0.124e0
(h)

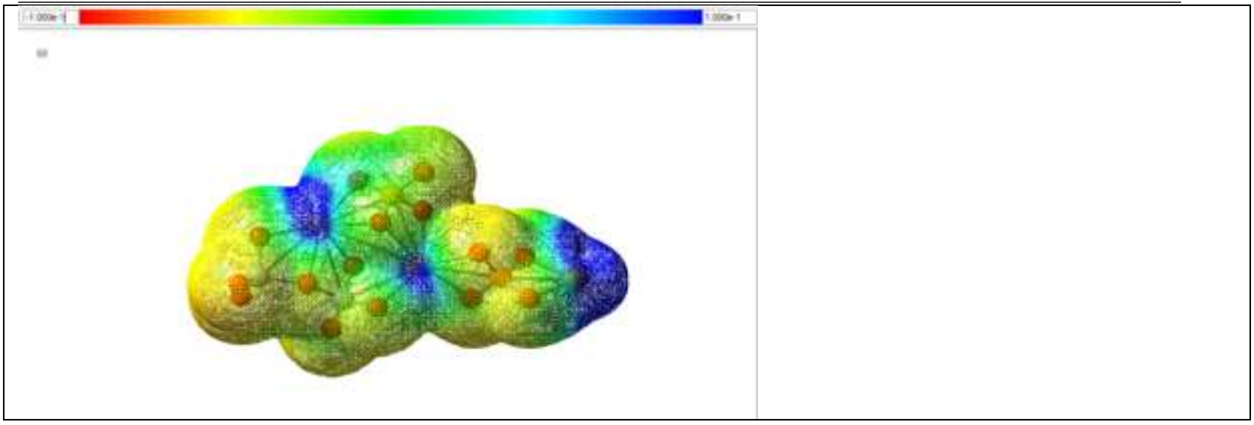

Figure 9. Electrostatic potential (ESP) surface maps visualization for (a) OB, (b) E122, (c) E124, (d) E129 (e) Cr(VI), (f) E122+OB, (g) E124+OB, (h) E129+OB, and Cr(VI)+OB based on the DFT/ B3LYP/6–31g (d, p) methodology. The spheres in blue and red correspond to the minimum and maximum of the ESP surface, respectively. Green and red represent the ESP varying from min to max level. ESP ranges are included in the legend at each figure panel.

2.4. Adsorption studies

2.4.1. Point of zero charge (pH_{PZC})

OB's pH_{pzc} was determined using a previously published approach [45]. **Fig.S3** demonstrates how the $pH_{initial}$ affects the shift in the OB's pH value ($pH_{initial}$-pH_{final}). It is found that pH_{PZC} of OB bisorbent value is 7.23. This demonstrates that the OB surface is regarded as positively charged at pH values lower than 7.23.

2.4.2. Effect of pH

The pH parameter should be carefully examined since the pH of the aqueous solution significantly affects the solid-liquid interactions due to surface functional group protonation–deprotonation. The influence of solution pH on removing Cr(VI), E122, E124, and E129 pollutants using OB was investigated in the range of 1.5–12. **Fig. S4.** illustrates that the OB adsorption efficiency decreased with increasing pH from 2.5 to 4. Finally, the adsorption efficiency of the investigated pollutants dropped at pH values higher than 5. From the calculation using the pH_{PZC} value (+ve < pH_{PZC} 7.3 >-ve). The OB surface is positive below pH_{PZC}, which permits the adsorption of the anionic contaminants. That is the main reason for increasing the adsorption of Cr(VI), E122, E124, and E129 at pH= (1.5-3) surface (The adsorption of the anionic dyes and chromate metal ion is facilitated by the acidic medium) [36].

2.4.3. Effect of adsorbent dose

The adsorbent dosage is one of the important factors because it presents the capacity of the adsorbent for a given initial concentration of the adsorbate. As shown in **Fig. S5**, with increasing the OB dose from 0.005 g to 0.03 g, the capacity of E122 adsorption reached its maximum at 86.76 mg/g, the capacity of the E124 adsorption reached its maximum at 180.4 mg/g, the capacity of the E129, adsorption reached its maximum at 85.66 mg/g, and the capacity of the Cr(VI) reached its maximum at 157.6 mg/g. With the rise in the dose above (0.01 g), it was observed that the capacity decreased for E122, E124, E129, and Cr(VI) adsorption. Since all of the active sites of the adsorbent surface are fully exposed at low adsorbent dosages, it is thought that the dispersion of OB particles in the bulk solution is better. This could hasten the approachability of pollutants' molecules to the majority of the adsorbent active sites. As a result, a large removal capacity is achieved by the adsorption on the surface-active sites, reaching a saturation threshold. However, at higher adsorbent dosages, the accessibility of adsorbent active sites with higher energy decreases, and a larger portion of active sites with lower energy become occupied, leading to a decrease in the adsorption process.

2.4.4. The effect of initial concentration of pollutants

Fig. 10A shows the outcomes of the studies that varied the starting concentrations of the pollutants under study (2.5–300 mg/L) over the OB samples. The adsorption capabilities rose in proportion to the initial pollutant concentrations, peaking at 200, 150, and 100 mg/L for Cr(VI), E122, [E124, and E129], respectively. Because of the interaction between the pollutants and the adsorbent, which provides the essential driving force to overcome the resistance to the mass transfer of pollutants across the aqueous solution and the bone samples, the loading capacities of OB biosorbent increase as pollutant concentrations rise. Furthermore, the following explanations could account for this phenomenon: The higher energy sites become saturated and adsorption starts on the lower energy sites, resulting in a decrease in adsorption efficiency (similar results have been previously published in the literature) [25]. At low pollutant/OB ratios, pollutant adsorption occurs on the high-energy sites.

2.4.5. Isotherm studies

Isotherm research: Utilizing Langmuir and Freundlich's isothermal models, the mechanism of E122, E124, and E129 adsorption onto the OB adsorbent was investigated. The equations of the two models are presented in **Eqs. (4), and (5)** in the experimental section. **Fig. 10 (b, d, f, h)** represents Langmuir, and **Fig. 10(c, e, g, i)** represents Freundlich plots for E122, E124, E129, and Cr(VI) adsorption. **Table 3** shows the parameters (q_m, K_L, R^2, n, K_F) of the two investigated isothermal models. From these results, the Langmuir isothermal model is well-matched with the three investigated dyes and metal adsorption as its constants are more related to the E122, E124, E129, and Cr(VI) adsorption processes with higher R^2. R^2 values for the Langmuir model are 0.99489, 0.99999, 0.99696, and 0.99847 for E122, E124, E129, and Cr(VI) removal, respectively, while R^2 values for the Freundlich model are 0.42546, 0.73017, 0.42144, and 0.8885 for E122, E124, E129, and Cr(VI) adsorption, respectively. Therefore, monolayer adsorption occurred in this instance. In addition, the estimated values of R_L are computed and found to be less than 1.00, suggesting that OB is a suitable material to use as an adsorbent for the investigated anionic species [26].

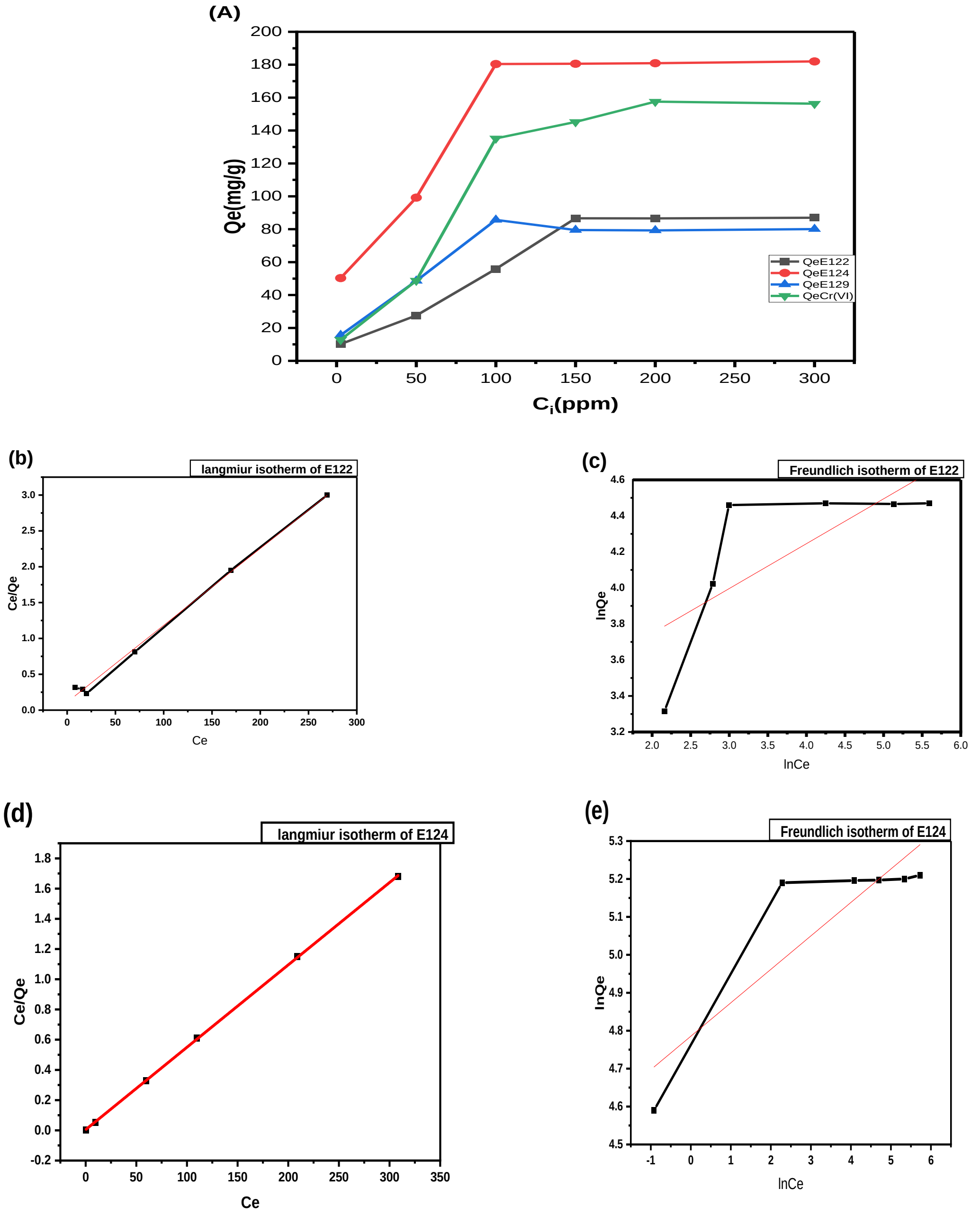

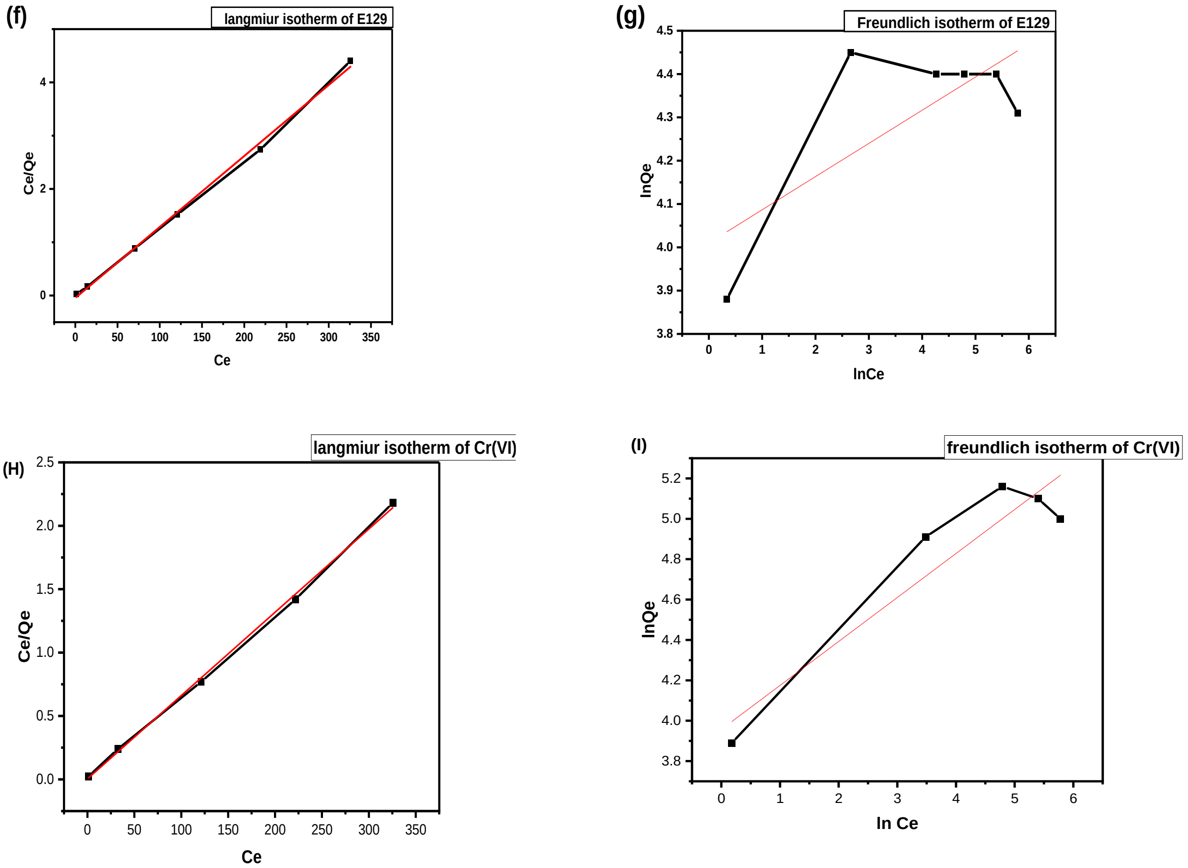

Figure 10. (A) The variation in dye and metal concentration in the OB adsorbent's adsorption capability. (B, D, F, H) represents the Langmuir isotherm, and (C, E, G, I) represent the Freundlich isotherm for the adsorption of the pollutants.

Table 3. The isotherm of Langmuir and the Freundlich isotherm models (conditions pH=1.5-2, [0.005gm for E124 and Cr(VI), 0.01 for E129, 0.015 for E122], and for 180min).

System	Langmuir isotherm constants			
	K_l	Q_m	R^2	R_L
OB+E122	0.0959	93.37	0.99489	0.0649
OB+E124	1.155	183.48	0.9999	0.008584
OB+E129	0.291	75.057	0.9969	-0.0356
OB+Cr(VI)	1.61	152.2	0.99847	0.003096
System	**Freundlich isotherm constants**			
	K_F	N	R^2	
OB+E122	25.8	4	0.425	
OB+E124	119.75	111.34	0.73017	
OB+E129	54.598	13.05	0.42144	
OB+Cr(VI)	52.3	4.59	0.8885	

2.4.6. Oscillation time and adsorption kinetic studies

The removal % of pollutants was investigated as a function of time (0.0–360 min) to determine the adsorption equilibrium time for the adsorption of E122 (150 mg/L), 100 mg/L of E124 and E129, and 200 mg/L of Cr(VI) onto OB (0.01 g) in a solution of pH 1.5 at 25 °C (**Fig. S6a**). In the beginning, the adsorption was very fast at 60 min, reaching 62.5mg/g for E122, 130.6mg/g for E124, 69.13mg/g for E129, and 120 mg/g for Cr(VI). Then, as the amount of time grew from 90 to 120 min, the removal efficiency increased from (75.5 to 86.67%), (from 76.6 to 90.2%) for E122 and E124, and (from 37.2% to 40%) for Cr(VI) respectively, while the E129 removal efficiency increased from 72.74 to 76.9% with shaking time increasing from 30 to 180 min. The efficiency remains constant when the shaking time is increased to more than 180 minutes for E129 and more than 120 minutes for E124/E129/Cr(VI). This indicates that the removal efficiency reached equilibrium at 180 minutes for Cr(VI), E124, and E129 and 120 minutes for E122. Towards the end of the experiment, the initial rapid adsorption gradually levels out (after 120 minutes), achieving equilibrium at a considerably lower rate (a dynamic equilibrium is reached between OB and the pollutants remaining in the liquid phase). Since there must have been more empty active sites available at the beginning, where the removal of the pollutants in the solution was completed in 180 minutes, the rapid adsorption at the initial stage is most likely caused by the increased concentration gradient across the adsorbate in solution and the adsorbent. A good water treatment system requires an understanding of the kinetics and mechanics of adsorption. The process is essentially controlled by the slowest stage, which occurs multiple times as the liquid solution is adsorbed onto the solid adsorbent surfaces. Data from the adsorption kinetic tests for various dye concentration solutions were used to simulate the linear form of the pseudo-first-order (PFO) and pseudo-second-order (PSO) models to investigate the sorption process of contaminants onto OB. **Table 4** lists their equation forms below.

The linearity plots of ln (qe–qt) vs time "t" for the pseudo-first-order (PFO) model were obtained, as shown in **Fig.S6 (b, d, f, h). Table 4** lists the adj. correlation coefficient (R^2) values, the kinetic parameter values of k_1, and qe, and the statistical parameters of fitting the (PFO) for pollutant adsorption. **Table 4** shows that the adsorption process did not proceed as the (PFO) model due to the lower adj. R^2 value and the larger statistical parameter values. Conversely, the linear forms of (PSO) equations' parameters highlighted that the solute-adsorption sites' chemical interaction at the adsorbent surface was the cause of the rate-limiting step. To comprehend the achievement of this approach, **Fig. S6 (c, e, g, i)** displays linear plots of t/q_t vs time "t" for various concentrations. The statistical parameters, adj-R^2, q_e, t, k_1, and k_2 were determined from the plots and included in **Table 4**. This table illustrates how the theoretical adsorption capacity (q_e) derived from the (PSO) model and the practical adsorption capacity (q_{exp}) are similar. Additionally, the statistical parameters have the lowest value (prob. value=0), and the adj. R^2 is likewise greater than 0.99 ($\sim$ 1). The pseudo-second-order model might describe the system.

To find the best-fitting model with E122, E124, E129, and Cr(VI) adsorption, researchers characterized two kinetic models: the pseudo-1st-order and the pseudo-2nd-order models (given in Eqs. (7) and (8), respectively). The estimated first- and second-order parameters (K_1, K_2, Q_{e1} ads, and Q_{e2} ads) and correlation coefficient R^2 values acquired from each examined model are shown in **Table 4** Adsorption kinetics parameters of E122, E124, E129, and Cr(VI) using OB System. When considering the pseudo-2nd order, the computed adsorption capacities of Cr(VI), E122, E124, and E129 were well-fitted with the experimental values. Besides, Comparing the pseudo-1st order R^2 values (0.76585 for E122, 0.91086 for E124, 0.57334 for E129, and 0.45467 for Cr(VI)) to the pseudo-2nd order R^2 values (0.98219 for E122, 0.98607 for E124, 0.98691 for E129, and 0.99006 for Cr(VI)), this shows R^2 values are higher in case of pseudo-second order. Hence, pseudo-1st-order theory is unable to account for the adsorption nature of this situation.

Table 4. The adsorption kinetics properties of the OB adsorbent for E122, E124, E129, and Cr(VI) (conditions pH=1.5-2, [0.005gm for E124 and Cr(VI), 0.01 for E129 0.015 for E122], and for 180min).

System	Pseudo 1st order		
	K_1(min^{-1})	Q_{e1ads}(mg/g)	R^2
OB-E122	20.035	94.07	0.76585
OB-E124	43.3	242.72	0.91086
OB-E129	9.379	85.32	0.57334
OB-Cr(VI)	-4.814	120.19	0.45467
System	Pseudo 2nd order		
	K_2 (g/(mg min)	Q_{e2ads}(mg/g)	R^2
OB-E122	0.0222	102.459	0.98219
OB-E124	$1.1986*10^{-4}$	222.2	0.98607
OB-E129	$2.299*10^{-5}$	91.5	0.98691
OB-Cr(VI)	$1.3777*10^{-4}$	197.63	0.99006

2.4.7. Temperature and Thermodynamic Studies

It was observed that when the temperature increased, the amount of E122, E124, E129, and Cr(VI) adsorption decreased, as shown in **Fig.S7A,** and this is due to when the adsorption process is exothermic, the physical adsorption occurs readily at low temperatures, and decreases with increasing temperature (Le-Chatelier principle). The thermodynamic parameters and K_c, the equilibrium constant, were calculated using **Eqs. (9) and (10)**. **Table 5** shows the estimated values of thermodynamic parameters, while **Fig. S7(b, c, d, e)** shows the plotted curves. The predicted negative ΔG° values demonstrate both the thermodynamic viability of the E122, E124, E129, and Cr(VI) adsorption within the examined temperature range and the spontaneous nature of the adsorption on OB adsorbent. Furthermore, the exothermic nature of the adsorption process is estimated by negative values of ΔH°. E122, E124, E129, and Cr(VI). Based on the high ΔH° values (> 80 kJ/mole), the adsorption was proposed to be chemisorption [36]. Furthermore, E122, E124, E129, and Cr(VI) adsorption leads to a decrease in randomness and an increase in alignment, as indicated by the negative ΔS° value.

Table 5. Thermodynamic parameters for the adsorption of E122, E124, E129, and Cr(VI) on OB adsorbent (conditions pH=1.5-2, [0.005gm for E124 and Cr(VI), 0.01 for E129 0.015 for E122], and for 180min).

Adsorption system	**K_c**			**ΔG^o (KJ/mol)**			**ΔH^o (KJ/mol)**	**ΔS^o(J/mol.K)**
	298K	**308K**	**318K**	**298K**	**308K**	**318K**		
OB+E122	4.338	1.637	1.048	-3.6346	-1.2624	-0.124	-72.9	-229.44
OB+E124	18.4	2.56	1.16	-7.18496	-2.41	-0.3923	-140.25	-446.71
OB+E129	5.97	1.73	1.01	-4.42742	-1.41	-0.026	-90.283	-288.178
OB+Cr(VI)	7.463	2.166	1.25	-4.979919	-1.979	-0.616	-90.3	-286.324

2.4.8. Effect of ionic strength

The ionic strength characteristic is regarded as significant since industrial wastewater contains high amounts of matrix. It was examined with several anions, including EDTA (0.1M,0.5M), NaCl (0.1, 0.5 M), KI (0.1M), $MgSO_4$(0.5M), Na_2CO_3 (0.1, 0.5 M), and $NaHCO_3$ (0.1, 0.5 M), at the optimum conditions of the investigated dye and metal adsorption. As shown in **Fig. S8**. E122, E124, E129, and Cr(VI) adsorption on the OB surface, the different anions at concentration 0.1 0.5M affect the investigated dye adsorption. In **Fig. S8 a**. the highest recovery of E122 was in the case of NaCl 0.5M (98.01), **Fig. S8b** E124 the highest recovery in the presence of NaCl 0.1M, Na_2CO_3 0.1M(75.76%), **Fig. S8c** E129 NaCl 0.5M (88.2%), and **Fig. S8d** the highest recovery of Cr(VI) by the use of $NaHCO_3$ (0.5M) reached 189.3%.

2.4.9. Desorption and Regeneration

The capacity of reuse of OB investigation of E122, E124, E129, and Cr(VI) adsorption-desorption was performed under ideal circumstances. Several eluents were investigated, and it was found that 0.5 M HCl is the best among them to recover E122, E124, Cr(VI), and $NaHCO_3$ 0.5M for E129, as shown in **Fig. S9.** Furthermore, due to the strong electrostatic bond formed between pollutant molecules and OB, it was hard to recover the dye and reuse OB.

2.4.10. Application

2.4.10.1. Analysis of real water samples

Depending on the previous results, the prepared OB was utilized to treat and decontaminate a real sample. The calibration curves were obtained using standard solutions. The 1.0 L standard solutions were made using the above-optimized experimental setup. The samples under investigation were seawater in Damietta City and tap water in our laboratory at Mansoura University. The obtained results are presented in **Table 6**. Not every sample contained every added dye naturally. The recoveries in the samples that were spiked with particular dye concentrations were determined. The recovered percentages ranged from 92.1% to 93.2%. These findings imply that OB adsorbent could be a useful tool for accurately determining the presence of pollutants in real water.

Table 6. The analytical results of adsorption of E122, E124, E129, and Cr(VI) in real water samples.

Sample	**Dye**	**Spiked ($\mu g.mL^{-1}$)**	**Measured ($\mu g.mL^{-1}$)**	**Recovery%**	**SD**	**RSD%**
Seawater	**E122**	150	95.7	41.72	0.1	0.1045
	E124	100	61.4	42.79	0.1	0.16286
	E129	100	35.5	75.414	0.1	0.283
	Cr(VI)	200	85.87	144.85	0.205	0.239
Tap-water	**E122**	150	30.24	91.8	0.1662	0.5498
	E124	100	49.9	55.5	0.153	0.306
	E129	100	44.7	64.58	0.089	0.201
	Cr(VI)	200	137.1	79.82	0.881	0.643
Wastewater	**E122**	150	44.9	80.73	0.153	0.34
	E124	100	20.1	77.54	0.153	0.508
	E129	100	19.5	93.94	0.153	0.782
	Cr(VI)	200	73.37	160.7	0.4687	0.6388

3.4.10.2. Analysis of dyes in colored soft drinks and candies

Various samples containing E122 and E129 were subjected to the optimal experimental conditions of E122 and E129 adsorption to assess the OB efficiency for anionic dye sorption. The standard solutions were used to create the calibration curves. Candy and degassed carbonated drinks were among the food samples. Candy (strawberry taste) was dissolved after being digested in 4% acetic acid, which includes E129 dye. As seen in **Table 7,** more than 71.23% for E122 and 61.969% for E129 in soft drinks, and 79.2% for E129 in candy were attained in the E122 and E129 recovery removal from the tested samples. These findings suggest that the recovery of these dyes from various materials might be effectively accomplished using the OB material.

Table 7. The analytical results of adsorption of E122 and E129 anionic dyes in real water soft drinks and candy using OB biosorbent (n=3).

Sample	Dye	C_i ($\mu g.mL^{-1}$)	Measured ($\mu g.mL^{-1}$)	Recovery%	SD	RSD%
Soft drink	E122	150	57.3	71.23	0.1	0.1745
Soft drink	E129	100	46.7	61.98	0.153	0.326
Candy	E129	100	32.15	79.21	0.05	0.155

2.4.11. Adsorption of pollutants in bi and multi-contaminated systems

2.4.11.1. UV-Visible spectra

For the mixture of two, three and four pollutants E122, E124, E129 and Cr(VI) which were studied at the conditions mentioned earlier, the UV–vis spectra of the different mixtures (E122+E124), (E124+E129), (E122+129), (E122+Cr(VI), (E124+Cr(VI), [(E129+Cr(VI)], [(E122+E124+E129), and [(E122+E124+E129+Cr(VI)]. **Fig.** 11(a–h) reflected that a new λ_{max} for each of the studied mixtures appeared that is not far away from the λ_{max} of the single pollutants (518nm for E122, 507nm for E124, 502nm for E129 and for 427nm Cr(VI), respectively) and but in between, which emphasized the equivalent selectivity toward the removal of the four pollutants in the binary and multicomponent systems at equilibrium time as shown in **Fig. 11** without forming an intermediate. This behavior demonstrated the adsorbent's lack of selectivity in adsorbing these four pollutants in the bi- and multi-adsorbate systems, in addition to revealing the adsorbent's higher affinity for them. This might be attributed to the similarity in their anionic nature. Further, the removal capacity of various mixed pollutants at the same conditions was close to Q_e for sole **E122, E124, E129, and Cr(VI)** (60- 229.3 mg/g). These results demonstrate that the produced adsorbent is qualified for water treatment, particularly in bi- and multi-adsorbate systems, since they demonstrated a very high removal efficiency for a mixture of anionic contaminants.

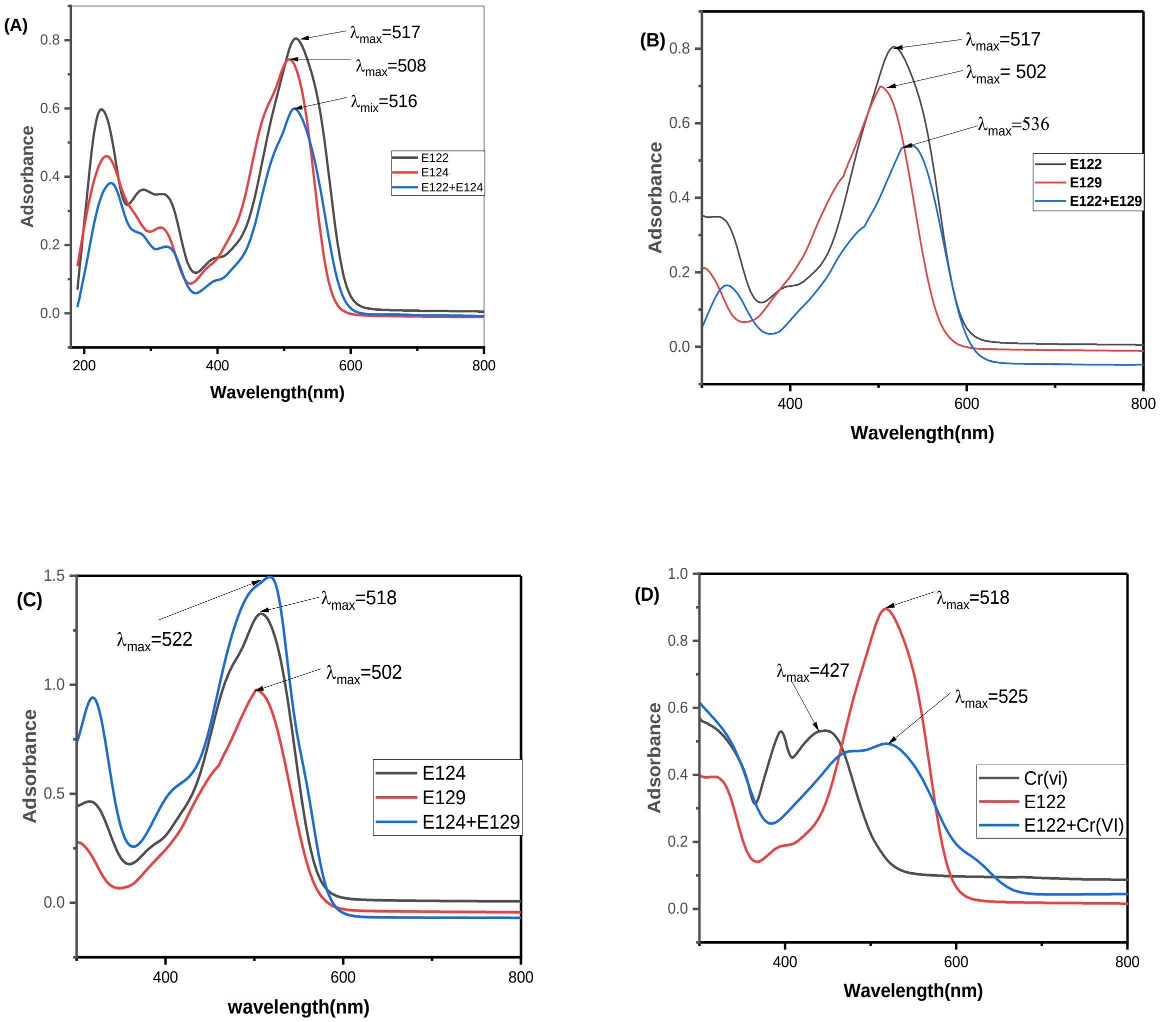

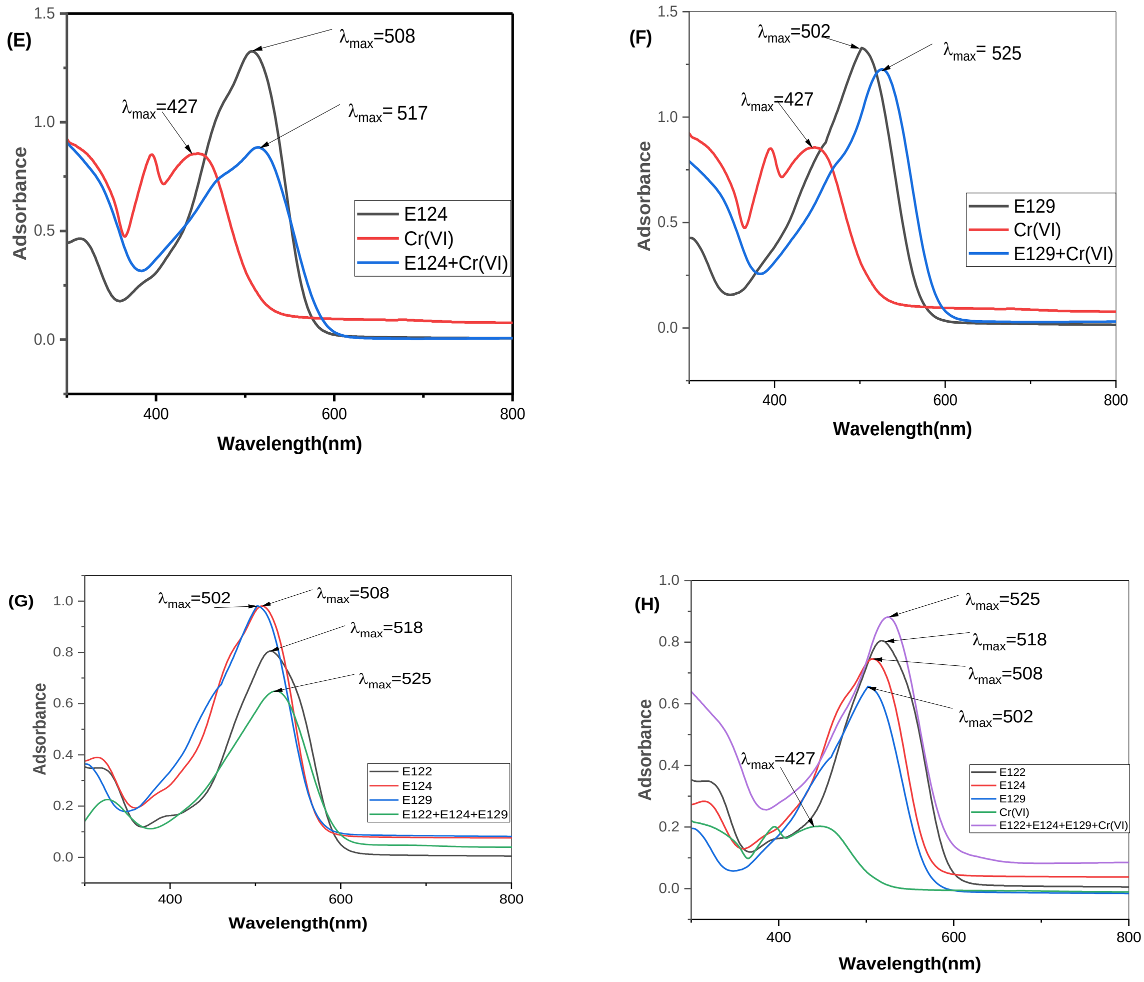

Figure 11. UV data of (A) E122+E124 mix is contrasted with E122 and E124, (B) E122+E129 mix is contrasted with E122 and E129, (C) E124+E129 mix is contrasted with E124 and E129, (D) Cr(VI)+E122 mix is contrasted with E122 and Cr(VI), (E) Cr(VI)+E124 mix is contrasted with Cr(VI) and E124, (F) Cr(VI)+E129 mix is contrasted with E129 and Cr(VI), (G) E122+E124+E129 mix is contrasted with E122, E124, and E129, and (H) E122+E124+E129 +Cr(VI) mix is contrasted with E122, E124, E129, and Cr(VI).

2.4.11.2. Kinetic studies for the multicomponent adsorption

It was necessary to apply OB biosorbent for the potential removal of (E122, E124, E129, Cr(VI)) at the previous new (λ_{max}) appeared in binary, tertiary, and mixed systems with different time intervals. For the adsorption experiment, 0.01 g of OB biosorbent was added to each system solution (75 mg/L E122, 50 mg/L of [E124, E129], and 100 mg/L Cr(VI)) at pH [1.5-2]. Then, the mixture was shaken at 150 rpm. The equilibrium concentration of the adsorbates was calculated from UV–Vis data. The adsorption efficiency of E122, E124, E129, and Cr(VI) was calculated by employing **Eq. (2).** As it can be noticed from **Fig. 12**, the absorbance, which is an indication of the dye's concentration, is markedly reduced with increasing time of adsorption denoting the efficient use of OB biosorbent for the removal of the investigated dyes in the binary system. It was observed from the calculation in **Table 8 and Fig.S10** that all of the multi-component systems follow pseudo-second-order by applying **Eq. (7&8).**

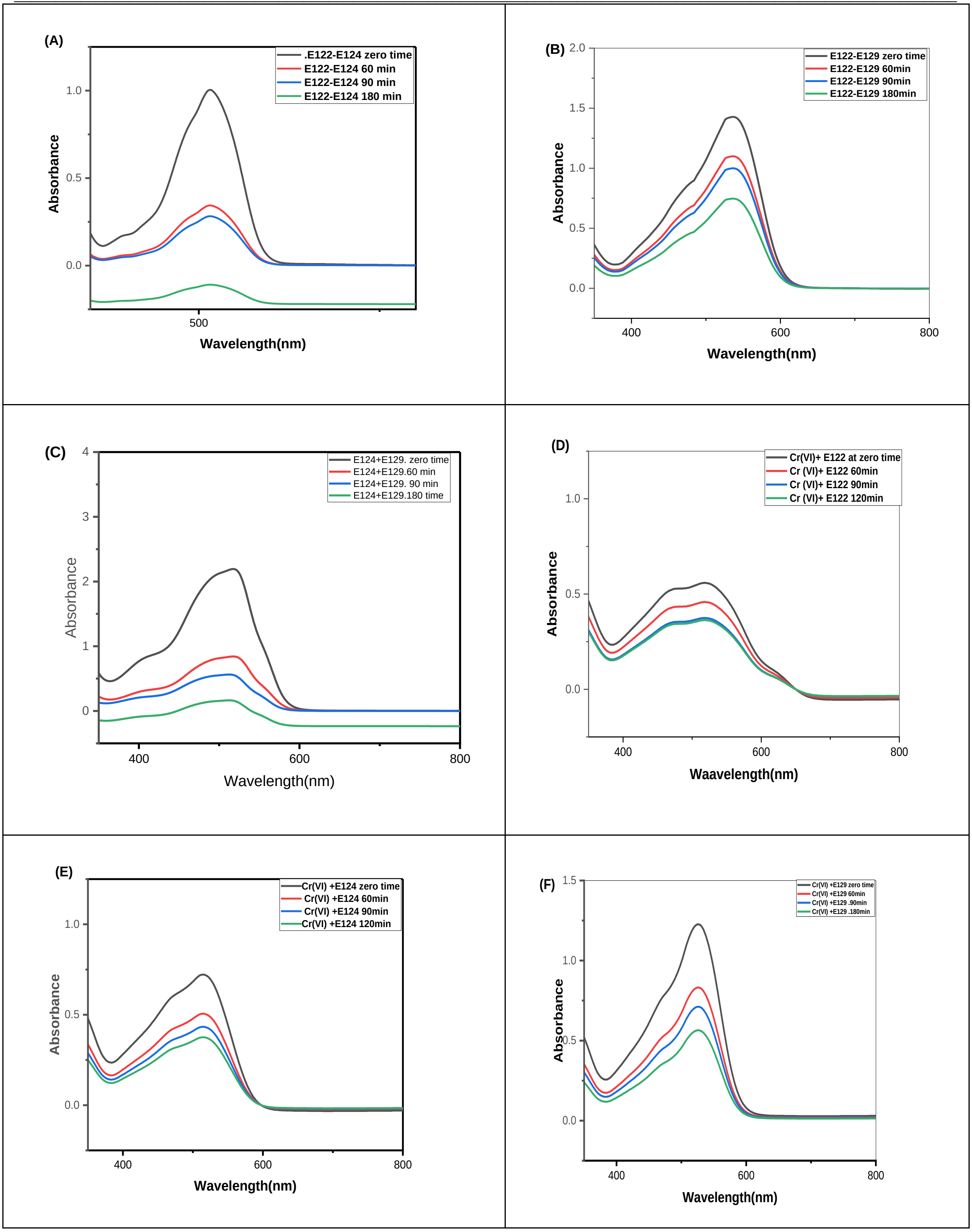
(A)
.E122-E124 zero time
E122-E124 60 min
E122-E124 90 min
E122-E124 180 min
Absorbance
1.0
0.5
0.0
500
Wavelength(nm)
(B)
2.0
1.5
1.0
0.5
0.0
E122-E129 zero time
E122-E129 60min
E122-E129 90min
E122-E129 180min
Absorbance
400
600
800
Wavelength(nm)
(C)
4
3
2
1
0
E124+E129. zero time
E124+E129.60 min
E124+E129. 90 min
E124+E129.180 time
Absorbance
400
600
800
Wavelength(nm)
(D)
Cr(VI)+ E122 at zero time
Cr (VI)+ E122 60min
Cr (VI)+ E122 90min
Cr (VI)+ E122 120min
1.0
0.5
0.0
Absorbance
400
600
800
Waavelength(nm)
(E)
Cr(VI) +E124 zero time
Cr(VI) +E124 60min
Cr(VI) +E124 90min
Cr(VI) +E124 120min
1.0
0.5
0.0
Absorbance
400
600
800
Wavelength(nm)
(F)
1.5
Cr(VI) +E129 zero time
Cr(VI) +E129 60min
Cr(VI) +E129 .90min
Cr(VI) +E129 .180min
1.0
0.5
0.0
Absorbance
400
600
800
Wavelength(nm)

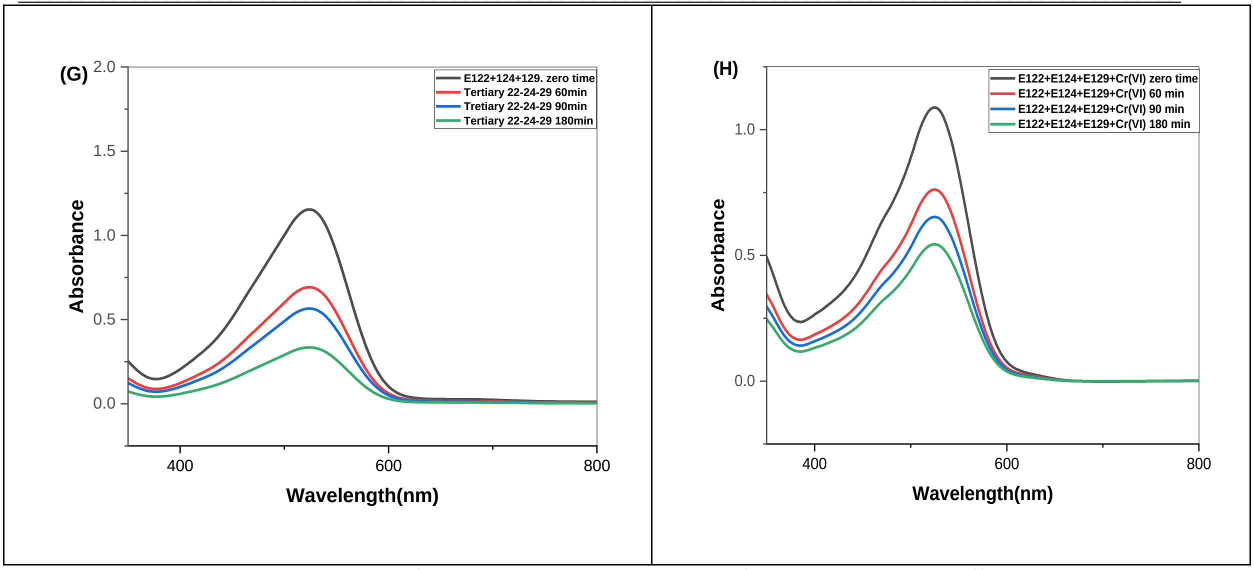

Figure 12. (A, B, C, D, E, F, G, H) UV data of E122, E124, E129, and Cr(VI) mix after adsorption by OB at different time intervals.

Table 8. Represents the adsorption kinetics properties of the OB adsorbent for multi-component system.

System	**Pseudo 1st order**		
	K$_1$(min^{-1})	**Q$_{e1ads}$(mg/g)**	**R^2**
E122-E124	40.73	135.5	0.96895
E122-E129	-5.45	37.1	0.10023
E129-E124	-1.9	71.9	0.0688
E122-Cr(VI)	-1.98	52.7	0.04038
E124-Cr(VI)	-2.081	58.96	0.0295
E129-Cr(VI)	0.1	78.125	0.7026
E122-E124-E129	-4.35	84.6	0.06746
E122-E124-E129-Cr(VI)	33.88	146.41	0.18879
System	**Pseudo 2nd order**		
	K$_2$ (g/(mg min)	**Q$_{e2ads}$(mg/g)**	**R^2**
E122-E124	0.000164	1388.5	0.9984
E122-E129	0.0000478	115.2	0.97357
E129-E124	0.00036	95.2	0.9973
E122-Cr(VI)	0.000413	72	0.99111
E124-Cr(VI)	0.0002355	89.85	0.98409
E129-Cr(VI)	0.0001217	111.235	0.99399
E122-E124-E129	0.000039	201.6	0.9772
E122-E124-E129-Cr(VI)	0.0000618	186.6	0.99266

2.4.11.3. Isotherm studies for a multi-component system

Solute-to-adsorbent molecule interactions in an adsorption system are necessary for the adsorption behavior. The equilibrium adsorbate concentrations in the solid and aqueous phases are referred to as isothermal at a particular temperature. Adsorption information, adsorption mechanisms, and a system's maximum adsorption capacity are all examined using isotherm equations, which are used to mimic the equilibrium adsorption data. The concentrations of the adsorbent in the solid phase and the adsorbate in the liquid phase are mathematically related thanks to isotherm equations, so at the same (λ_{max}) for the previous mixed systems we measured the isothermal capacity of OB to adsorb the pollutants in the multi-component system for different concentrations as shown in **Fig. 11S** using the extended Langmuir and Freundlich models **Eq [11, 12]** to analyze the isotherm data in a multi-component system [46, 47]] This resulted in the multi-component system follows Langmuir isotherm as it has the more related value of Qe with an (R^2) about 0.9984 for all systems as illustrated in **Table 9** and the value of (R$_L$) is an evidence that the reaction is reversible.

$$\mathbf{q_i = \frac{q_{m,i}.K_L C_i}{1+\sum_{j=1}^{n} K_{l,j}.C_j}} \quad (11)$$

$$\mathbf{\ln q_i = \ln K_i + \frac{1}{n} \ln C_i} \quad (12)$$

Table 9. Represents the isotherm of OB adsorption in a multi-component system.

System	Langmuir isotherm constants			
	K_l	Q_m	R^2	R_L
E122-E124	2.18	56.85	0.99803	0.007587
E122-E129	0.443	67.73	0.99605	0.0274
E129-E124	2.99	77.8	0.99983	0.00416
E122-Cr(VI)	0.968	67.3	0.99811	0.013
E124-Cr(VI)	0.251	93.1	0.98392	0.0475
E129-Cr(VI)	0.5786	75.3	0.99196	0.0211
E122-E124-E129	1.618	70.17	0.9964	0.007668
E122-E124-E129-Cr(VI)	3.11	84.1	0.97345	0.0039997
System	Freundlich isotherm constants			
	K_F	N	R^2	
E122-E124	35.87	6.35	0.60735	
E122-E129	27.7	4.51	0.9488	
E129-E124	44.55	3.97	0.8184	
E122-Cr(VI)	37.96	6.02	0.91648	
E124-Cr(VI)	18.8	2.16	0.85409	
E129-Cr(VI)	44	6.3	0.95377	
E122-E124-E129	45.6	8	0.93454	
E122-E124-E129-Cr(VI)	51.41	4.5	0.69086	

2.4.12. The adsorption mechanism

Several mechanisms can be considered in an attempt to account for the adsorption of pollutants with particular structural features. Included in these are the following:

1) Chelation: of surface calcium by bidentate ligands formed possibly from the functional groups -NH and C O, -OH and C~-O, or --N~ and --OH. This occurs mainly in the tris medium.
2) Hydrogen bonding: between the dye molecule's ionized carbonyl oxygen and the hydroxyl groups in hydroxyapatite or azo-nitrogen, -NH-. In calcium-deficient apatite, these hydroxyl groups in hydroxyapatite may even be found as a component of the orthophosphate groups [48]. Preferential adsorption, perhaps by hydrogen bonding, followed by chemisorption of dye onto the alcohol. This has been found on the surface of many adsorbents such as alumina and silica [49], but it is unknown to which atoms in hydroxyapatite ethanol might attach themselves. Incidentally, claimed that tris, which behaves as a cation at pH 7.4, was not adsorbed by synthetic hydroxyapatite [50].
3) Electrostatic interaction: a replacement of surface (or hydration shell) phosphate by negatively charged groups in the dye molecule and the negative charge of $(Cr_2O_7)^{2-}$, particularly sulphonate (--SO_3^-), permitting attachment of the dye and chromate through these groups. There may be complex formation or adsorption in which the union resembles an acid-base reaction or salt formation, with negatively charged groups on dye and chromate molecules linked with positively charged surface calcium. In the anthraquinonoid dyes, there is evidence that union with calcium can occur at the 2-hydroxyl position.
4) The plausible mechanism of adsorption of the three anionic dyes is represented in **Fig. 13a,** and **Fig. 13b** is the mechanism for Cr(VI) adsorption.

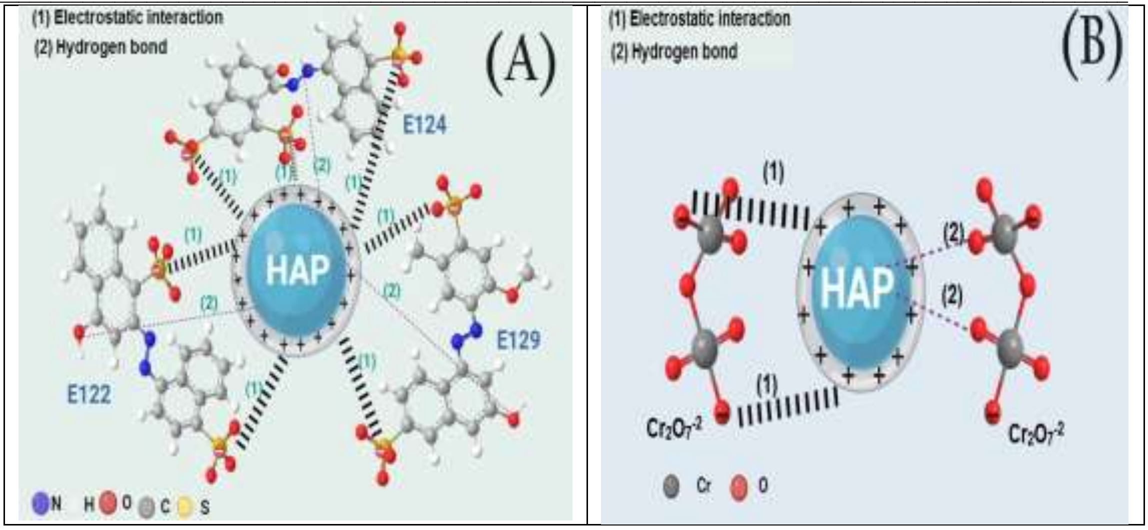

Figure 13. (A) the interaction between OB and the three anionic dyes, and **(B)** the interaction between OB biosorbent and Cr(VI).

2.4.13. Performance of OB biosorbent

E122, E124, E129, and Cr(VI) anionic species can be effectively separated and removed from a variety of water samples using the OB Biomaterial. A comparison of the OB performances with those of the other mentioned adsorbents is shown in **Table 10**. It was noted that OB biomaterial should take into account the sorption capacity, type, dose, beginning concentration, and equilibrium duration of the sorption while comparing various adsorbents for the remediation of E122, E124, E129, and Cr(VI). Finally, **Table 10** shows that, in comparison to the other adsorbents described, the OB has excellent capacities and efficiencies for the E122, E124, E129, and Cr(VI) recovery.

Table 10. The comparison of the adsorption capacity of E122, E124, E129, and $K_2Cr_2O_7$ onto OB with previously reported studies.

Adsorbate	Adsorbent	Adsorbent dose	Initial concentration (mg/L)	Equilibrium time	q_e (mg/g)	References
E122	OB	0.015g	150	120 min	86.76	Current study
	$ZrSiO_4$NPsCTAB@Fe_3O_4 NPs-DoTAB	0.005g	100	20 min	66.5	[51]
	ND	1g/L	50	60 min	12	[52]
	Doped (Ag)ZnO$_{NPS}$	0.08g	5	80 min	84.7	[53]
	$0.1SnO_2$–$0.9CeO_2$	1g/L	20	20 min	22.10	[54]
	$0.15SnO_2$–$0.85CeO_2$				22.8	
	$0.2SnO_2$–$0.8CeO_2$				21.16	
	$0.3SnO_2$–$0.7CeO_2$				18.33	
	Bt@CTAB	0.4g/L	100	240 min	248.75	[55]
E124	OB	0.005g	100	120 min	180.4	Current study
	Fe_3O_4@SiO_2 -CMK-8, MNCs	0.1g	50	20 min	78.74	[56]
	NH_2-MMNC	0.008g	50	30 min	58.8	[57]
	Bt@CTAB	٠,٤g/L	150	240 min	358.25	[55]
E129	OB	0.01g	100	12 min	85.66	Current study
	Activated carbon	400mg	3	96 h	72.85	[58]
Cr(VI)	PPy/MoS_2	0.015 g/50 mL	50	24 h	257.73	[59]
	Coffee grounds and Mixed waste tea	5g	100	120 min	94.34 (coffee ground) 87.72 (Mixed waste tea)	[60]
	A-RS/PVA	0.01 g/20 mL	100	48 h	140.39	[61]
	OB	0.005g	200	120 min	157.67	Current study
	CS@CTAB	0.005g	100	120 min	490.196	[36]

3. Experimental

3.1. Proposed computational approach

Density functional theory (DFT) provides accurate and reliable information about the electrical characteristics, vibrational frequency, rotational barrier, and shape of the compounds. The Ostrich Bone (OB) unit was used to carry out geometry improvements and additional DFT calculations., E122, E124, E129, Cr(VI), these anionic dyes, and Cr(VI) with product Ostrich Bone. DFT is considered a cost-effective method to approximate electron correlation effects. All DFT calculations were performed by using the B3LYP level of theory, Becke's three-parameter (B3) nonlocal exchange with the correlation functional of Lee, Yang, and Parr (LYP) [62]. Nowadays, the B3LYP level is currently widely used to study organic electronic compounds because the predicted geometries are very reliable and provide good estimations for HOMO–LUMO gaps, in good agreement with experimental values [63–68]. All the calculations for geometry optimizations were carried out at the B3LYP/6–31g(d,p) for all atoms. All computations were carried out by using the Gaussian09 suite of programs [69]. IR spectrum was graphed using the GaussSum2.2.5 program [70], and full natural bond orbital (NBO) analyses were made to calculate the charge distribution for all molecules by using NBO version 3.1 [71]. Gauss View 5.0 package [72] was employed to produce several graphic depictions of the unique molecular orbitals' forms. Important ideas in theoretical molecular design include the minimal unoccupied molecular orbital (LUMO) and a highly occupied molecular orbital (HOMO) [73]. Through Koopman's theorem [74], the HOMO and LUMO orbital energies can be used to predict the electronic characteristics and reactivity descriptors, such as ionization potential (IP), electron affinity (EA), hardness (η), softness (σ), and electronegativity (χ).

The Global Reactivity Descriptors (GRD): Ionization potential (I_P), electron affinity (E_A), electronegativity (χ), global hardness η) softness (σ), can be explained in terms of the energy of the HOMO and the LUMO, are shown in **Table S1** [75-80].

3.2. Materials

The pristine Ostrich bone waste (OB), which includes the leg and breast bones, was used in this paper after being purchased from a local store and dried, crushed, and sieved. The chemical structure of OB and pollutants is illustrated in **Fig. 14.** NaOH (98%), EDTA (99.995%), $NaHCO_3$ (99.5%), HCl (37%), NaCl (99%), Na_2CO_3 (99.5%), ethanol (99.9%), Ponceau 4R ($C_{20}H_{11}N_2Na_3O_{10}S_3$, E124), Azorubine ($C_{20}H_{12}N_2Na_2O_7S_2$, E122), and Red Alora (80%) ($C_{18}H_{14}N_2Na_2O_8S_2$, E129) anionic food dyes, and $K_2Cr_2O_7$ (99.9%) are the substances that are utilized. These were all analytical-grade compounds that were purchased from Sigma-Aldrich. The chemical structures of the studied pollutants are shown in **Fig. 14**.

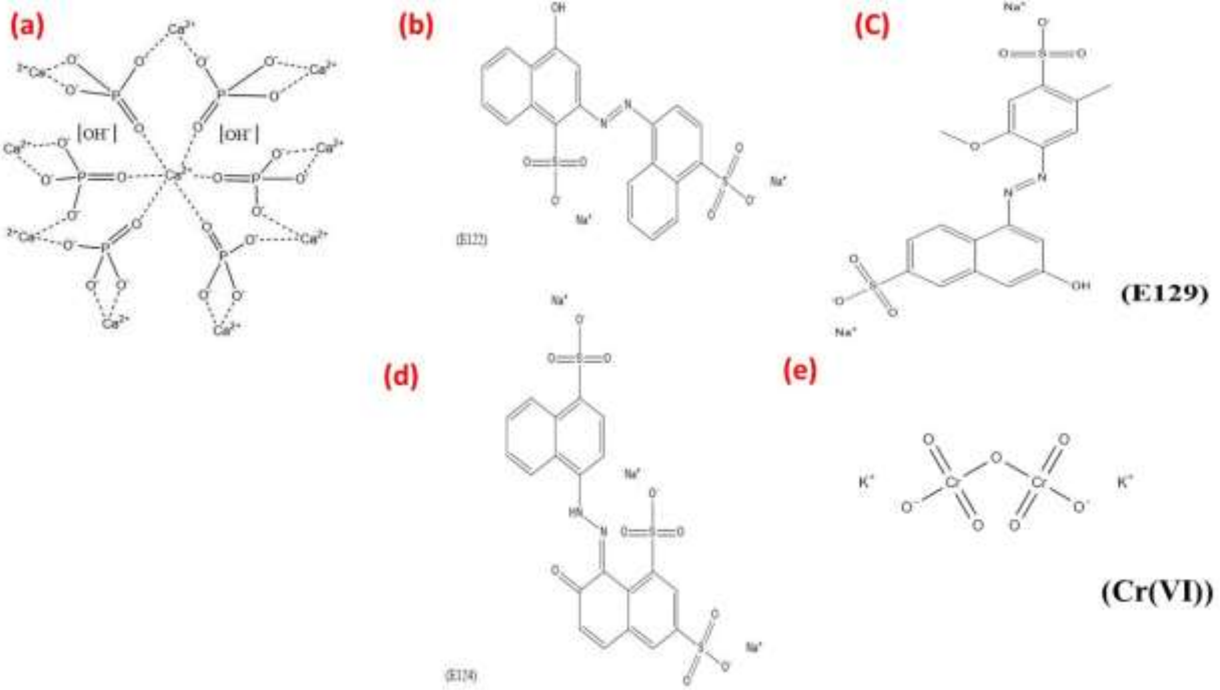

Figure 14. (a) The chemical structure of hydroxyapatite [$Ca_{10}(PO_4)_6(OH)_2$], (b, c, d, and e) E122, E129, E124, Cr(VI), respectively.

3.3. Characterization

By employing a Perkin-Elmer 550 spectrophotometer, the concentration of each of the investigated systems was measured across a wavelength range of 200–900 nm. The maximum absorption wavelengths (λ_{max}) recorded were 518 nm for E122, 508 nm for E124, 501 nm for E129, and 427nm for Cr(VI). The FTIR spectra of OB biosorbent, OB-E122, OB-E124, OB-E129, and OB-Cr(VI) were characterized by (Perkin-Bhaskar-Elmer Co., USA). The surface morphology of prepared materials was examined using the JSM-6510LV model. The specific surface area of the prepared material was determined through Brunauer–Emmett–Teller (BET) analysis using a Size Analyzer (QUANTACHROME–NOVA 2000 Series). Thermogravimetric analysis (Perkin Elmer TGA 4000) was used to determine thermal stability at a 15 °C/min heating rate from 30 to 800 °C. X-ray diffraction (XRD) patterns of the OB sample were obtained using an Analytical Pert PRO diffractometer spanning the 2-theta (2θ) range from 4° to 70°. The pH at the point of zero charge (pH_{PZC}) of OB was determined through the following procedure: 0.1 gram of the OB adsorbent was mixed with 25 milliliters of NaCl solution (0.01 M) adjusted to various pH levels ranging from 2 to 12. The mixtures were then shaken on an equilibrated shaker for 48 hours. The pH adjustment of the NaCl solution was achieved using 0.1 M HCl and 0.1 M NaOH. After shaking, the final pH was recorded, and the difference in pH (ΔpH) was calculated using the equation $\Delta pH = pH_i - pH_f$, where pH_i represents the initial pH and pH_f is the final pH. The point where the ΔpH curve plotted against pHi intersects the line ΔpH = 0 was identified as the pH_{PZC} value [55].

3.4. Adsorption and regeneration procedures

3.4.1. Batch tests

By scanning the solutions throughout the range of 190-1100 nm, the absorption spectra (λ_{max}) of E122, E124, E129, and Cr(VI) were obtained. The maximum absorption wavelengths were 518 nm for E122, 508 nm for E124, 501 nm for E129, and 427nm for Cr(VI) [81]. Adsorption studies of these dyes were carried out at values between 25 and 400 mg/L. A contaminated solution (10 mL) and a dose of adsorbent OB (0.01 g) were added to 25 mL stoppered bottles for the adsorption experiments. The bottles were shaken at room temperature at 150 rpm using a thermostatic shaker. Upon reaching equilibrium, the solutions underwent a 3000rpm centrifugation. The solution that remained after adsorption and contained traces of the contaminants under investigation was evaluated at the particular λ_{max} for all pollutants. Samples were regularly scanned between 200 and 900 nm after adsorption to find the lambda maximum. Several parameters were investigated, including contact time (ranging from 30 to 180 minutes), temperature (between 25 and 45 °C), OB adsorbent dosage (from 0.005 to 0.03 grams), and initial concentration of the pollutant (50–400 mg/L), ionic strength, and pH levels (varying from 1.5 to 11) Pollutant removal percentage (R, (%)) and adsorption capacity (q_e) of pollutants were calculated as per **Eqs. (1) and (2)**, respectively [45].

$$R\% = \frac{Ci-Cf}{Ci} \times 100 \qquad (1)$$

$$qe = \frac{(Ci-Cf)\times v(l)}{wt} \times 100 \qquad (2)$$

C_i (mg/L) and C_f (mg/L) are the initial and equilibrium concentrations, respectively. Where wt (g) is the OB dose and V (L) is the amount of pollutant under study.

3.4.2. Desorption and regeneration studies

The desorption of the pollutants under investigation was tested using various eluents, such as NaOH (0.1 mol/L), sodium bicarbonate (0.5 mol/L), ethanol, and HCl (0.5,0.3,0.1 mol/L), following the adsorption of anionic dyes E122, E124, E129, and metal ion Cr(VI) by OB. Using the batch approach, the adsorption-desorption was used to investigate the regeneration of OB. The absorbent was filtered before being eluted with HCl (0.5 mol/L) for [E122, E124, and Cr(VI)] and $NaHCO_3$ (0.5 mol/L) for E129. After shaken with dosage (0.015, 0.005, 0.01g of OB) for [E122, (E124, Cr(VI)), E129], respectively with 10 mL of (150 mg/LE122), (100 mg/L for E124 and E129), and (200 mg/L of Cr(VI) for 120 min for E122, E124, E129, and Cr(VI). The desorption (D, %) of the pollutants under investigation from OB biosorbent was computed using **Eq. (3)** [18].

$$Desorption\ (\%) = \frac{amount\ of\ desorbed\ to\ the\ solution\ (mg/L)}{amount\ adsorbed\ on\ OB\ (mg/L)} \times 100 \qquad (3)$$

3.4.3. Kinetics, isotherm, and thermodynamics studies

3.4.3.1. Impact of initial concentration and isotherm studies

The investigations concerning isotherms for E122, E124, E129, and Cr(VI) adsorption were performed by placing (0.015, 0.005, 0.01g) Doses of OB adsorbent in a range of bottles comprising E122, [E124, Cr(VI)], and E129 solution. The initial concentration of the contaminant was between 50 and 400 mg/L. For E129, E124, E122, and Cr(VI) at pH 1.5, these bottles were shaken at 150 rpm for 120 minutes at 25 °C in a thermostatic shaker. The parameters were determined using Freundlich's and Langmuir's isothermal models, as indicated by **Eqs. (4) and (5),** respectively. One crucial parameter is the Langmuir separation factor (R_L), which is shown in **Eq. (6).** It is used in adsorbent-sorbate affinity prediction. The following explanation applies to the indications of R_L values: While values between 0 and 1 reflect the acceptability of the adsorbent utilized, R_L greater than 1.0 indicates that the adsorbent under examination is inappropriate [45].

$$\frac{\mathrm{Ce}}{\mathrm{Qe}} = \frac{1}{\mathrm{K_l q_m}} + \frac{\mathrm{C_e}}{\mathrm{q_m}} \qquad (4)$$

$$\ln \mathrm{Q}_e = \ln\mathrm{K}_f + \frac{1}{\mathrm{n}}\ln C_e \qquad (5)$$

$$R_l = \frac{1}{1+K_l C_\circ} \qquad (6)$$

As C_e (mg/L) is the anionic dyes (E122, E124 and E129) and Cr(VI) concentration at equilibrium, q_e (mg/g) is the pollutant capacity at equilibrium, q_m (mg/g) is the adsorption mum amount, The heterogeneity factor is represented by 1/n, and the Langmuir and Freundlich constants are K_L (L/mg) and K_F (mg/g), respectively.

3.4.3.2. Impact of contact time and kinetics studies

Two kinetic models, pseudo-1st-order and pseudo-2nd-order, were used in kinetic experiments to predict the adsorption rate-limiting phase. These models were reported in **Eqs. (7) and (8)**. Studies were carried out at the ideal pH for pollutants using 10 mL150 mg/L of E122, (100 mg/L of E124,200 mg/L of Cr(VI)), and 100 mg/L of E129 [0.015, 0.005, and 0.01 g] in order of the OB adsorbent. These pollutants were allowed to shake with varying contact times from 30 to 180 minutes in a thermostatic shaker at room temperature at a constant speed of 150 rpm [82].

$$\frac{1}{Q_t} = \frac{k_1}{q_{et}} + \frac{1}{q_e} \qquad (7)$$

$$\frac{t}{q_t} = \frac{1}{k_2 q_e^2} + \frac{t}{q_e} \quad (8)$$

The adsorption efficiency for investigated pollutants at equilibrium and at a certain time t (min) is expressed as q_e (mg/g) and q_t (mg/g), respectively. K_1 and K_2 are constants for pseudo-1st order and pseudo-2nd-order, respectively.

2.4.3.3. Effect of temperature and thermodynamics

10 mL of the anionic dyes' solution (100 mg/L for E124 and E129 and 150 mg/L for E122) and 10 mL of 200 mg/L Cr(VI) with an ideal pH of (1.5-2) were shaken for 120 minutes for E122, E124, Cr(VI), and E129 in a set of 25-mL stoppered flasks containing these dosages (0.015, 0.005, and 0.01 g) of OB at different temperatures (25–45) °C. Following filtering and adsorption, the residual dye concentration (E122, E124, and E129) and metal concentration were measured. As stated in **Eqs. 9 and 10** and computed as follows, the thermodynamic parameters (adsorption enthalpy (ΔH°), adsorption free energy (ΔG°), and adsorption entropy (ΔS°); from **Eq. (10)** intercept that equals ΔS°/R and slope that equals −ΔH°/R of Ln Kc vs. 1/T. A gas constant expressed as (R) equals 8.314 J/mol K [51].

$$\Delta G^o = \text{-}RT\ln K_C \quad (9)$$

$$\ln Kc = \frac{\Delta S^o}{R} - \frac{\Delta H^o}{RT} \quad (10)$$

3.4.3.4. Error analysis

Using the Levenberg–Marquardt iteration technique included in the OriginPro 2019 program, the study's unknown parameters for the kinetic and isotherm models were obtained. The above kinetic and isotherm models were evaluated for fitting quality using the adjusted coefficient of determination (Adj. R^2) [6].

3.5. Application

3.5.1. Analysis of real water samples

The real water samples were spiked with different concentrations of the studied pollutants viz. 100 mg/L of (E124, E129), 150 mg/L of E122 and 200 mg/L of Cr(VI). Before the dyes were spiked, the actual water samples were fully digested by adding 0.5 g of $K_2S_2O_8$ and 5 mL of H_2SO_4 98% (w/w) to 1000 mL of the water sample. The mixture was then heated for 120 min at 90 °C to fully dissolve the organic compounds that were present. The samples were allowed to cool to room temperature before being mixed with 0.01 g of OB biosorbent and continuously shaken for 120 min with the pH level down to 1.5–2. To guarantee total separation, the solutions were centrifuged once more, and 0.01 g of OB biosorbent was added to the supernatant. The remaining amount of E122, E124, E129, or Cr(VI) employing an Ultraviolet-visible Unicam UV 2100 spectrometer at the proper wavelengths.

3.5.2. Elimination of dyes from industrial samples and colored soft beverages

To remove E122 and E129 from degassed carbonated beverages and candy, OB was utilized. In the beginning, the carbonated drinks (a strawberry beverage with E129 dye and a watermelon beverage with E122 dye) were degassed by leaving them in the air at 25 °C for 120 min. After being digested (which means the breakdown of unwanted substances in the candy sample) using acetic acid (4%), the strawberry candy was dissolved. For E122 and E129, OB dosage (0.015, 0.01 g) was introduced to each sample, and the optimum pH for each dye was set with constant shaking for 180 min. Using the Unicam UV 2100 UV/Visible spectrometer at the proper wavelengths, the residual E122 and E129 were identified.

Conclusion

Finding affordable pollutants-binding adsorbents is essential to efficient water treatment. The results of the present investigation show that:

a- Pristine Ostrich Bone is a potentially highly applicable biosorbent in removing anionic food dyes from water (E122, E124, and E129) and metal ion chromate from water samples.
b- The pH, reaction temperature, and beginning concentration affected the adsorption of the anionic food dyes E122, E124, E129, and Cr(VI).
c- Langmuir adsorption isotherms on a homogeneous surface provide a good description of the homeostasis of the adsorption process. An almost second-order kinetic model is used in the kinetic investigations.
d- Thermodynamic parameters indicate that it's a spontaneous, exothermic chemisorption reaction.
e- Isotherm and kinetics of a multicomponent system.
f- In this work, the prepared OB biosorbent has high efficiency of anionic food dye removal and chromate ion (Cr^{6+}) removal at optimal batch sorption conditions, with an upper limit on the sorption capacity of 86.67 mg/g, 180.4 mg/g, 85.9 mg/g, and 157.67 mg/g, respectively, mg. g^{-1} for E122, E124, E129, and Cr(VI), that was achieved in 90–120 minutes. The anionic food dyes E122, E124, E129, and chromate ions (Cr^{6+}) were removed using the prepared biosorbent (OB) in both single and multi-component dye solution modes.
g- The prepared OB biosorbent was successfully used to remove E122, E124, E129, and Cr(VI) from natural water and industrial food samples:
h- Submersion of the OB dye sample in 10 mL of HCl 0.5 m and $NaHCO_3$ resulted in the desorption of about (99.9-90.5%) of E122, E124, and (140%) of Cr(VI), and about 24.4% for E129 dyes.
i- DFT calculations were performed on the Ostrich Bone (OB) unit, E122, E124, E129, Cr(VI), these anionic dyes, and Cr(VI) with product Ostrich Bone.
j- The adsorption mechanism was proposed to be due to electrostatic interaction (between Ca(II) of hydroxyapatite and dyes SO_3 group, and oxygenated group in chromate) and the formation of the hydrogen bond.
k- In conclusion, the present work demonstrated the potential of this technique for environmental remediation well.

l- The process of synthesis, characterization, adsorption, and DFT studies of pristine OB for the removal of studied pollutants is graphically represented in **Fig. 15.**

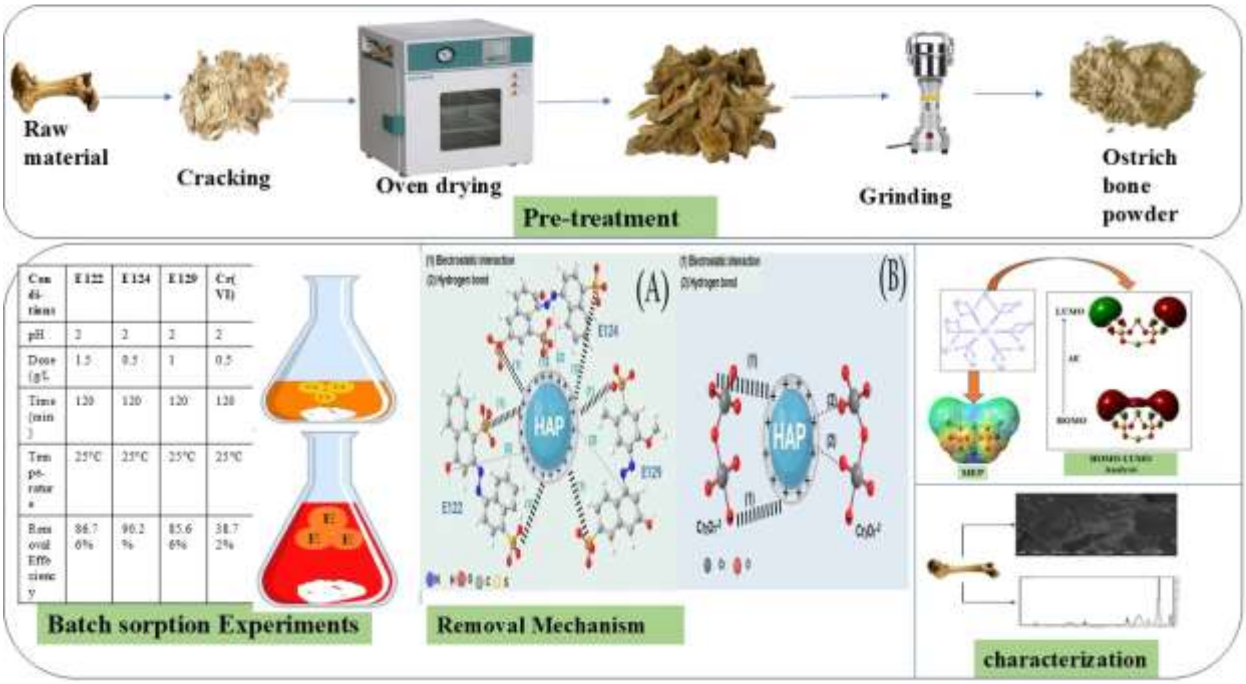

Conditions	E122	E124	E129	Cr(VI)
pH	2	2	2	2
Dose (g/L	1.5	0.5	1	0.5
Time (min)	120	120	120	120
Temperature	25°C	25°C	25°C	25°C
Removal Efficiency	86.76%	90.2 %	85.66%	38.72%

Figure 15. Graphical abstract that represents the study of OB and the removal of pollutants.

Declarations

Ethics approval and consent to participate: Not applicable to this study. Consent for publication: Not applicable to this study
Availability of data and materials: All data generated or analyzed during this study are included in this published article
Competing interests: The authors declare that they have no competing interests."
Funding: This research didn't receive external funding
Authors' contributions:
Doha MM Elawady: Investigation, Writing – original draft, review
Elsayed RH El-Gharkawy: Conceptualization, Methodology, Investigation, Writing – original draft, review, Supervision
Magda A Akl**:** Supervision, Conceptualization, Methodology, Investigation, Writing – original draft, review

Acknowledgments: Not applicable to this study.

References

[1] Nathanson, J. A. (2024). Water pollution. Encyclopedia Britannica.
[2] Brudzyńska, P., Sionkowska, A., & Grisel, M. (2021). Plant-derived colorants for food, cosmetic and textile industries: a review. Materials 14: 3484.
[3] Benkhaya, S., M'rabet, S., Lgaz, H., El Bachiri, A., & El Harfi, A. (2022). Dyes: classification, pollution, and environmental effects. Dye biodegradation, mechanisms, and techniques: Recent advances, 1-50.
[4] Ritchie, H., & Roser, M. (2024). FAQs on plastics. Our World in Data.
[5] Islam, T., Repon, M. R., Islam, T., Sarwar, Z., & Rahman, M. M. (2023). Impact of textile dyes on health and ecosystem: A review of the structure, causes, and potential solutions. Environmental Science and Pollution Research, 30(4), 9207-9242
[6] Dikshit, R., & Tallapragada, P. (2018). Comparative study of natural and artificial flavoring agents and dyes. In Natural and artificial flavoring agents and food dyes (pp. 83-111). Academic Press
[7] Leulescu, M., Iacobescu, G., Bojan, M., & Rotaru, P. (2019). Ponceau 4R azoic red dye: Thermal behavior, optical anisotropy, and terahertz spectroscopy study. Journal of Thermal Analysis and Calorimetry, 138, 2091-2101.
[8] Bakthavachalu, P., Kannan, S. M., & Qoronfleh, M. W. (2020). Food color and autism: a meta-analysis. Personalized Food Intervention and Therapy for Autism Spectrum Disorder Management, 481-504.
[9] Umar. F, Misbahul.A .K, Makshoof. A Janusz A. Kozinski, (2011), Effect of modification of environmentally friendly biosorbent wheat (Triticum aestivum) on the biosorption removal of cadmium (II) ions from aqueous solution, Chemical Engineering Journal, Volume 171, Issue 2, 1 July 2011, Pages 400–410
[10] Hu, Q., Pei, Q., Zhang, Y., Pang, S., & Feng, C. (2024). Facile preparation of oxygen vacancy-rich magnesium oxide for advanced removal of phosphate from aqueous solutions. Journal of Water Process Engineering, 66, 106080.

[11] Waranusantigula, P, Pokethitiyook, P, Kruatrachue, M, Upatham, E.S, (2003), Kinetics of basic dye (methylene blue) biosorption by giant duckweed (Spirodela polyrrhiza), Environmental Pollution 125, 385–392

[12] Mohan.D and Pittman. C.U, Activated carbons and low-cost adsorbents for remediation of tri- and hexavalent chromium from water, J. Hazard. Mater. B. 137 (2006) 762–811

[13] Ibrahim, A., El Fawal, G. F., & Akl, M. A. (2019). Methylene blue and crystal violet dye removal (as a binary system) from aqueous solution using local soil clay: kinetics study and equilibrium isotherms. Egyptian Journal of Chemistry, 62(3), 541-554.Bal, G., & Thakur, A. (2022). Distinct approaches of removal of dyes from wastewater: A review. Materials Today: Proceedings, 50, 1575-1579.

[14] Söğüt, E. G., & Gülcan, M. (2023). Adsorption: basics, properties, and classification. In Adsorption through Advanced Nanoscale Materials (pp. 3-21). Elsevier.

[15] Shen, L. Y., Tam, V. W., Tam, L., & Ji, Y. B. (2010). Project feasibility study: the key to successful implementation of sustainable and socially responsible construction management practice. Journal of Cleaner Production, 18(3), 254-259.

[16] He, H., Meng, X., Yue, Q., Yin, W., Gao, Y., Fang, P., & Shen, L. (2021). Thiol-ene click chemistry synthesis of a novel magnetic mesoporous silica/chitosan composite for selective Hg (II) capture and high catalytic activity of spent Hg (II) adsorbent. Chemical Engineering Journal, 405, 126743.Conti, S., Sala, G., & Mateus, O. (2023). Smart Biomechanical Adaptation Revealed by the Structure of Ostrich Limb Bones. Biomimetics, 8(1), 98.

[17] Hong, M. H., Lee, J. H., Jung, H. S., Shin, H., & Shin, H. (2022). Biomineralization of bone tissue: calcium phosphate-based inorganics in collagen fibrillar organic matrices. Biomaterials Research, 26(1), 42.

[18] Kini, U., & Nandeesh, B. N. (2012). Physiology of bone formation, remodeling, and metabolism. Radionuclide and hybrid bone imaging, 29-57.

[19] Isaeva, V. I., Vedenyapina, M. D., Kurmysheva, A. Y., Weichgrebe, D., Nair, R. R., Nguyen, N. P. T., & Kustov, L. M. (2021). Modern carbon-based materials for adsorptive removal of organic and inorganic pollutants from water and wastewater. Molecules, 26(21), 6628.

[20] Arshadi, M., Ghosh, J. E., Zandi, H., & Foroughifard, S. (2015). Phosphate removal by a nano-biosorbent from the synthetic and real (Persian Gulf) water samples. RSC Advances, 5(54), 43290-43302.

[21] Stathopoulou E. T., Psycharis V., Chryssikos G. D., Gionis V., and Theodorou.G., Palaeogeogr., Palaeoclimatol., Palaeoecol., 2008, 266, 168. Bone diagenesis: New data from infrared spectroscopy and X-ray diffraction

[22] Arshadi M. , Salimi Vahid F., J. W. L. Salvacion and M. Soleymanzadeh, Appl. Surf. Sci., 2013, 280, 726.

[23] Ibrahim, A. R., Li, X., Zhou, Y., Huang, Y., Chen, W., Wang, H., & Li, J. (2015). Synthesis of spongy-like mesoporous hydroxyapatite from raw waste eggshells for enhanced dissolution of ibuprofen loaded via supercritical CO2. International journal of molecular sciences, 16(4), 7960-7975.

[24] Arshadi .M, Shakerib *a H. and Salvacionb. J. W. L. A green adsorbent for the removal of BTEX from aqueous media† RSC Adv., 2016, 6, 14290

[25] Geiker NRW, Bertram HC, Mejborn H, Dragsted LO, Kristensen L, Carrascal JR, Bügel S, Astrup A. Meat and Human Health-Current Knowledge and Research Gaps. Foods. 2021 Jul 5;10(7):1556. doi: 10.3390/foods10071556. PMID: 34359429; PMCID: PMC8305097.

[26] Hart, A., Porbeni, D. W., Omonmhenle, S., & Peretomode, E. (2023). Waste bone char-derived adsorbents: characteristics, adsorption mechanism, and model approach. Environmental Technology Reviews, 12(1), 175–204.

[27] Flores-Cano JV, Leyva-Ramos R, Carrasco-Marin F, et al (2016) Adsorption mechanism of Chromium (III) from water solution on bone char: Effect of operating conditions. Adsorption 22:297–308

[28] Nageeb RM, Abd-Elmenaim Gad A, Fathy NM (2019) Adsorption of Cd (II) and Pb (II) using physically pretreated camel bone biochar. Adv J Chem-Sect A 2(4):347–364

[29] Rojas-Mayorga CK, Silvestre-Albero J, Aguayo-Villarreal IA (2015) A new synthesis route for bone chars using CO_2 atmosphere and their application as fluoride adsorbents. MicroporousMesoporous Mater 209:38–44

[30] Mendoza-Castillo DI, Bonilla-Petriciolet A, Ja Jauregui-Rinco NJ (2015) On the importance of surface chemistry and composition of bone char for the sorption of heavy metals from aqueous solution. Desalin Water Treat 54:1651–1662

[31] Reynel-Avila HE, Mendoza-Castillo DI, Bonilla-Petriciolet A (2015) Assessment of naproxen adsorption on bone char in aqueous solutions using batch and fixed-bed processes. J Mol Liq 209:187–195

[32] Reynel-Avila HE, Mendoza-Castillo DI, Bonilla-Petriciolet A (2016) Relevance of anionic dye properties on water decolorization performance using bone char: adsorption kinetics, isotherms and breakthrough curves. J Mol Liq 219:425–434

[33] El Haddad, M., Slimani, R., Mamouni, R., ElAntri, S., & Lazar, S. (2013). Removal of two textile dyes from aqueous solutions onto calcined bones. Journal of the Association of Arab Universities for Basic and Applied Sciences, 14(1), 51-59.

[34] Ammar H.Y and E. R. H. El-Gharkawy, European Journal of Scientific Research, Vol.120 No.3 (2014), pp.401-415.

[35] Veligeti, R., Ramakrishna, D. S., Madhu, R. B. & Anireddy, J. S. Synthesis of fluoro and trifuoromethyl substituents containing novel tetracyclic N-benzylated benzopiperazine fused acridone regioisomers using a greener solvent 2-MeTHF and their DFT studies. J. Fluor. Chem. 257–258, 109989 (2022).

[36] Mostafa, A. G., Gaith, E. A. & Akl, M. A. Aminothiol supported dialdehyde cellulose for efficient and selective removal of Hg (II) from aquatic solutions. Sci. Rep. https://doi.org/10.1038/s41598-023-46082-3 (2023).

[37] Pearson, R.G., 2005. The Principle of Maximum Hardness. Chemical Hardness, (2): 99–124.

[38] Reed, A.E., L.A. Curtiss and F. Weinhold, 1988. Intermolecular Interactions from a Natural Bond Orbital, Donor-Acceptor Viewpoint. Chemical Reviews, 88(6): 899–926.

[39] Parr R.G., Donnelly R.A., Levy. M., Palke. W.E, Electronegativity - Density Functional Viewpoint, J Chem Phys, 68 (1978) 3801-3807.

[40] Chakraborty.T, Gazi. K, Ghosh. D.C, Computation of the atomic radii through the conjoint action of the effective nuclear charge and the ionization energy, Mol. Phys. 108 (16) (2010) 2081–2092.

[41] Asadi. Z, Esrafili. M.D, E. Vessally, M. Asnaashariisfahani, S. Yahyaei, A. Khani, A structural study of fentanyl by DFT calculations, NMR and IR spectroscopy, J. Mol. Struct. 1128 (2017) 552–562.

[42] Rana, M. M., Akhtar, N., Rahman, M. S., Hasan, M. Z., & Asaduzzaman, S. M. (2017). Extraction and characterization of hydroxyapatite from bovine cortical bone and effect of radiation. International Journal of Biosciences, 11(3), 20-30.

[43] Sarkar, A., Mushahary, N., Basumatary, F., Das, B., Basumatary, S. F., Venkatesan, K., ... & Basumatary, S. (2024). Efficiency of montmorillonite-based materials as adsorbents in dye removal for wastewater treatment. Journal of Environmental Chemical Engineering, 12(3), 112519.

[44] Akl, M. A., Mostafa, A. G., Abdelaal, M. Y. & Nour, M. A. K. Surfactant supported chitosan for efficient removal of Cr(VI) and anionic food stuff dyes from aquatic solutions. Sci. Rep. 13(1), 15786. https://doi.org/10.1038/s41598-023-43034-9 (2023).

[45] Rajendran, S. (2017). Influence of potassium dichromate-Zn2+ system on corrosion inhibition of rebar steel in simulated concrete pore solution. JOURNAL OF ADVANCED APPLIED SCIENTIFIC RESEARCH, 1(9).

[46] Swenson, H., & Stadie, N. P. (2019). Langmuir's theory of adsorption: A centennial review. Langmuir, 35(16), 5409-5426.

[47] Allen, S. J., & Brown, P. A. (1995). Isotherm analyses for single component and multi-component metal sorption onto lignite. Journal of Chemical Technology & Biotechnology: International Research in Process, Environmental AND Clean Technology, 62(1), 17-24.

[48] Speirs, R. L. (1970). The reaction between some dyes and synthetic hydroxyapatite I. The uptake of dyes about their structures. The Histochemical Journal, 2, 45-66.

[49] Nabil, G. M., Mahmoud, M. E., & Makled, S. O. (2023). Green synthesis of novel magnetite mixed metal oxides with cationic surfactant nanocomposite: Investigation of its effective removal of Azorubine E122 food dye and antimicrobial activity. Applied Organometallic Chemistry, 37(4).

[50] Labiod, K. et al. Removal of azo dye carmoisine by adsorption process on diatomite. Adsorption. Sci. Technol. 2022, 1–17.

[51] Hamada, M. S. & Jabal, R. A. Doped (Ag) ZnO nanoparticles for removal of azo dyes from aqueous solutions. Int. J. Chem. Biochem. Sci 21, 210–217 (2022).

[52] Ali, I. et al. Preparation and characterization of SnO2-CeO2 nanocomposites: Sorption, modeling, and kinetics for azorubine dye removal in water. J. Mol. Liquids 346, 117119. https://doi.org/10.1016/j.molliq.2021.117119 (2022)

[53] Toutounchi S, Shariati S, Mahanpoor K (2021) Application of magnetic ordered mesoporous carbon nanocomposite for the removal of Ponceau 4R using factorial experimental design. SILICON 13:1561–1573

[54] Sojoudi M, Shariati S, Khabazipour M (2016) Amine functionalized kit-6 mesoporous magnetite nanocomposite as an efficient adsorbent for removal of Ponceau 4R dye from aqueous solutions. Iran Chem Soc Anal Bioanal Chem Res 3:287–298

[55] Mostafa, A. G., Abd El-Hamid, A. I., & Akl, M. A. (2023). Surfactant-supported organoclay for removal of anionic food dyes in batch and column modes: adsorption characteristics and mechanism study. Applied Water Science, 13(8), 163

[56] Alkahtani, S. A., Abu-Alrub, S. S., & Mahmoud, A. M. (2017). Adsorption of food coloring Allura red dye (E129) from aqueous solutions using activated carbon. International Journal of Food and Allied Sciences, 3(1), 10-19.

[57] Xiang, L. et al. Polypyrrole-coated molybdenum disulfide composites as adsorbent for enhanced removal of Cr(VI) in aqueous solutions by adsorption combined with reduction. Chem. Eng. J. 408, 127281. https://doi.org/10.1016/j.cej.2020.127281 (2021).

[58] Cherdchoo, W., Nithettham, S. & Charoenpanich, J. Removal of Cr(VI) from synthetic wastewater by adsorption onto coffee ground and mixed waste tea. Chemosphere 221, 758–767. https://doi.org/10.1016/j.chemosphere.2019.01.100 (2019).

[59] Lin, C. et al. A study on adsorption of Cr(VI) by modified rice straw: Characteristics, performances, and mechanism. J. Clean. Prod. 196, 626–634. https://doi.org/10.1016/j.jclepro.2018.05.279 (2018).

[60] Sobhanardakani, S., Parvizimosaed, H., & Olyaie, E. J. E. S. (2013). Heavy metals removal from wastewater using organic solid waste—rice husk. Environmental Science and Pollution Research, 20, 5265-5271.

[61] Atif, M., Haider, H. Z., Bongiovanni, R., Fayyaz, M., Razzaq, T., & Gul, S. (2022). Physisorption and chemisorption trends in surface modification of carbon black. Surfaces and Interfaces, 31, 102080.

[62] El-Gharkawy E. R. H and H. Y. Ammar, Journal of Nanoelectronics and Optoelectronics Vol. 13 (2018), pp. 546–553.

[63] Carvalho M. N., da Motta M., Benachour.M, Sales D. C. S. and Abreu C. A. M., Hazard .J. Mater., 2012, 239– 240, 95. Chin C. J. M., Shih L. C., Tsai H. J. and Liu. T. K, Carbon, 2007, 45, 1254.

[64] Zhu, W., & Wu, P. (2004). Surface energetics of hydroxyapatite: a DFT study. Chemical Physics Letters, 396(1-3), 38-42

[65] Soria-Martínez, R., Longuinho, M., & Rossi, A. M. (2024). Non-covalent interactions and adsorption affinities of doxycycline and tetracycline with the (010) and (001) surfaces of hydroxyapatite. A DFT and experimental study. Surfaces and Interfaces, 46, 104010.

[66] Akl M.A, El-Mahdy N.A and. El-Gharkawy ES.R.H, Sci Rep 12, (2022) 17451.

[67] Frisch M. J, G. W. Trucks, H. B. Schlegel, G. E. Scuseria, M. A. Robb, J. R. Cheeseman, G. Scalmani, V. Barone, B. Mennucci, G. A. Petersson, H. Nakatsuji, M. Caricato, X. Li, H. P. Hratchian, A. F. Izmaylov, J. Bloino, G. Zheng, J. L. Sonnenberg, M. Hada, M. Ehara, K. Toyota, R. Fukuda, J. Hasegawa, M. Ishida, T. Nakajima, Y. Honda, O. Kitao, H. Nakai, T. Vreven, J. A. Montgomery, Jr., J. E. Peralta, F. Ogliaro, M. Bearpark, J. J. Heyd, E. Brothers, K. N. Kudin, V. N. Staroverov, T. Keith, R. Kobayashi, J. Normand, K. Raghavachari, A. Rendell, J. C. Burant, S. S. Iyengar, J. Tomasi, M. Cossi, N. Rega, J. M. Millam, M. Klene, J. E. Knox, J. B. Cross, V. Bakken, C. Adamo, J. Jaramillo, R. Gomperts, R. E. Stratmann, O. Yazyev, A. J. Austin, R. Cammi, C. Pomelli, J. W. Ochterski, R. L. Martin, K. Morokuma, V. G. Zakrzewski, G. A. Voth, P. Salvador, J. J. Dannenberg, S. Dapprich, A. D. Daniels, O. Farkas, J. B. Foresman, J. V. Ortiz, J. Cioslowski, and D. J. Fox, Gaussian, Inc., Wallingford CT (2013).

[68] O'Boyle N. M., A. L. Tenderholt, K. M. Langner. J. Comp. Chem., 29 (2008) 839.

[69] Glendening E. D., Reed A. E, Carpenter J. E, Weinhold.F., NBO version 3.1.

[70] Dennington, R., Keith, T. and Millam, J. (2009) Gauss View, Version 5. Semichem Inc., Shawnee Mission.

[71] Shoba, D., S. Periandy, M. Karabacak and S. Ramalingam, 2011. Vibrational spectroscopy (FT-IR and FT-Raman) investigation, and hybrid computational (HF and DFT) analysis on the structure of 2,3-naphthalene diol. Spectrochimica Acta - Part A: Molecular and Biomolecular Spectroscopy, 83(1): 540–552.

[72] Koopmans .T, Über die Zuordnung von Wellenfunktionen und Eigenwerten zu den Einzelnen Elektronen Eines Atoms, Physica, 1 (1934) 104-113.

[73] Wang. H, Wang.X , Wang.H, Wang. L, Liu A., DFT study of new bipyrazole derivatives and their potential activity as corrosion inhibitors, J. Mol. Model. 13 (1) (2007) 147–153.

[74] Pauling.L, The Nature of the Chemical Bond and the Structure of Molecules and Crystals: An Introduction to Modern Structural Chemistry, Cornell University Press, 1960.

[75] Senet. P, Chemical harnesses of atoms and molecules from frontier orbitals, Chem. Phys. Lett. 275 (5) (1997) 527–532.

[76] Parr. R. G, Szentpaly. L.V, Liu.S, Electrophilicity index, J. Am. Chem. Soc. 121 (9) (1999) 1922–1924.

[77] Chattaraj. P.K., Sarkar. U, Roy. D.R., Electrophilicity index, Chem. Rev. 106 (6) (2006) 2065–2091.

[78] Gomez. B, Likhanova.N.V, M.A. Dominguez-Aguilar, R. Martinez-Palou, A. Vela, J.L. Gazquez, Quantum chemical study of the inhibitive properties of 2-pyridylazoles, J. Phys. Chem. B 110 (18) (2006) 8928–8934.

[79] Chojnacka, K. (2005). Equilibrium and kinetic modeling of chromium (III) sorption by animal bones. Chemosphere, 59(3), 315-320.

[80] Saha, N., Volpe, M., Fiori, L., Volpe, R., Messineo, A., & Reza, M. T. (2020). Cationic dye adsorption on hydro chars of winery and citrus juice industries residues: Performance, mechanism, and thermodynamics. Energies, 13(18), 4686.

[81] Abd-Elhamid, A.I., Mostafa, A.G., Nayl, A.A. Akl, M.A. Novel sulfonic groups grafted sugarcane bagasse biosorbent for efficient removal of cationic dyes from wastewater. Sci Rep 14, 19129 (2024). https://doi.org/10.1038/s41598-024-60193-5

[82] Praveen, P. L., DS, R., & Ojha, D. P. (2017). UV spectral characterization of a smectic-C liquid crystal: theoretical support to the experiment. Molecular Crystals and Liquid Crystals, 643(1), 76-82.